



Article

Aerosols over East and South Asia: Type Identification, Optical Properties, and Implications for Radiative Forcing

Yushan Liu ¹ and Bingqi Yi ^{1,2,*}

¹ School of Atmospheric Sciences and Guangdong Province Key Laboratory for Climate Change and Natural Disaster Studies, Sun Yat-sen University, Guangzhou 510275, China; liuysh6@mail2.sysu.edu.cn

² Southern Marine Science and Engineering Guangdong Laboratory (Zhuhai), Zhuhai 519082, China

* Correspondence: yibq@mail.sysu.edu.cn

Abstract: Identification of aerosol types has long been a difficult problem over East and South Asia due to various limitations. In this study, we use 2-dimensional (2-D) and multi-dimensional Mahalanobis distance (MD) clustering algorithms to identify aerosol characteristics based on the data from the Aerosol Robotic Network from March 1998 to February 2018 over the South and East Asian region (10°N~50°N, 70°E~135°E). The single scattering albedo (SSA), absorption Angstrom exponent (AAE), extinction Angstrom exponent (EAE), real index of refraction (RRI), and imaginary index of refraction (IRI) are utilized for classification of aerosols. Sub-regions with similar background conditions over East and South Asia are identified by hierarchical clustering algorithm to illustrate distinctive meteorological states in different areas. The East and South Asian aerosols are found to have distinct regional and seasonal features relating to the meteorological conditions, land cover, and industrial infrastructure. It is found that the proportions of dust aerosol are the highest in spring at the SACOL site and in summer at the sites near the Northern Indo-Gangetic Plain area. In spring, biomass-burning aerosols are dominant over the central Indo-China Peninsula area. The aerosol characteristics at coastal sites are also analyzed and compared with previous results. The 2-D clustering method is useful when limited aerosol parameters are available, but the results are highly dependent on the sets of parameters used for identification. Comparatively, the MD method, which considers multiple aerosol parameters, could provide more comprehensive classification of aerosol types. It is estimated that only about 50% of the data samples that are identifiable by the MD method could be classified by the 2-D methods, and a lot of undetermined data samples could be mis-classified by the 2-D methods. The aerosol radiative forcing (ARF) and the aerosol radiative forcing efficiency (ARFE) of various aerosol types at the top and the bottom of the atmosphere (TOA and BOA) are determined based on the MD aerosol classification. The dust aerosols are found to have the largest ARF at the TOA (-36 W/m^2), followed by the urban/industrial aerosols and biomass-burning aerosols. The ARFE of biomass-burning aerosols at the BOA ($-165 \text{ W/m}^2 / \text{AOD}_{550\text{nm}}$) is the strongest among those of the other aerosol types. The comparison of the results by MD and 2-D methods shows that the differences in ARF and ARFE are generally within 10%. Our results indicate the importance of aerosol type classification in accurately attributing the radiative contributions of different aerosol components.

Keywords: aerosol classification; 2-dimensional clustering; Mahalanobis distance; hierarchical clustering; radiative forcing



Citation: Liu, Y.; Yi, B. Aerosols over East and South Asia: Type Identification, Optical Properties, and Implications for Radiative Forcing. *Remote Sens.* **2022**, *14*, 2058. <https://doi.org/10.3390/rs14092058>

Academic Editors: Simone Lolli, Kai Qin, Jason Blake Cohen and Davide Dionisi

Received: 16 March 2022

Accepted: 23 April 2022

Published: 25 April 2022

Publisher's Note: MDPI stays neutral with regard to jurisdictional claims in published maps and institutional affiliations.



Copyright: © 2022 by the authors. Licensee MDPI, Basel, Switzerland. This article is an open access article distributed under the terms and conditions of the Creative Commons Attribution (CC BY) license (<https://creativecommons.org/licenses/by/4.0/>).

1. Introduction

Atmospheric aerosols, which refer to liquid or solid particles suspended in the atmosphere, are key components of the earth's atmosphere. The atmospheric aerosols stem from natural and anthropogenic sources consisting of primary particulate matter (sea salt, mineral dust, and black carbon) and secondary aerosols from gaseous precursors (ammonium, nitrate, and sulphate) [1–5].

The atmospheric aerosols play an important role in perturbing the regional and global climate, as well as in inducing the environmental change [6–10]. For example, heavy precipitation and intense lightning were found to occur more frequently under polluted conditions than under clean conditions in the Pearl River Delta region [11]. Black carbon and sulfate aerosols in China were found to weaken the East Asian monsoon both in summer and winter, while their impacts on the vertical structures of atmospheric circulation and temperature profiles differ [12]. Jiang et al. [13] found that smoke aerosols tend to inhibit convection while continental aerosols from pollution tend to invigorate convection over South America, Central Africa and Southeast Asia. Improving the understanding of the aerosol types, distributions, optical properties, and radiative impacts are vitally important to understanding the impacts of aerosols on weather and climate.

Ground-based measurements focusing on global or regional aerosols, such as Aerosol Robotic Network (AERONET) [14], the China Aerosol Remote Sensing Network (CARSNET) [15], and Sun-sky radiometer Observation NETwork (SONET) [16], provide a reliable basis for aerosol classification which involves the use of technical methods like pattern identification and clustering analysis [17–21]. Bibi et al. [21] analyzed the discrimination of aerosol types including dust, urban/industrial (U/I), and biomass-burning (BB) aerosols by multiple clustering approaches using AERONET datasets in the northern Indo-Gangetic plain, and found that they were in good agreement with the CALIPSO (the Cloud-Aerosol Lidar and Infrared Pathfinder Satellite Observation) satellite retrieval products. Hamill et al. [17] analyzed the aerosol characterization at ~200 AERONET sites based on the Mahalanobis distance method which yields several aerosol models of urban/industrial, biomass-burning, dust, marine, and mixed types. Li et al. [18] used 18 aerosol microphysical parameters at 16 sites from the multi-year SONET data set to generate 10 typical clusters including five fine models and five coarse models in the China region by aerosol clustering analysis. Zheng et al. [19] obtained eight typical aerosol models in the North China Plain based on the Angstrom exponent and single scattering albedo by using CARSNET data. It can be seen that there are ample successful attempts to classify aerosol types from ground-based remote sensing measurements.

The radiative effect of aerosol is defined as the changes in radiative flux due to the combined absorption and scattering of radiation by atmospheric aerosols [22–26]. The aerosol radiative effects are also regarded as important indicators of the impacts of aerosols on the climate. The influence of aerosol–radiation interaction was found to decrease the direct component of the incident solar radiation at the surface by 20–30% at all seasons over the European region from a modeling perspective [27]. Wang et al. [28] reported remarkable changes in radiative fluxes and atmospheric temperature profile in the modeling study of a typical dust storm process, and they further found that direct radiative effects of dust aerosols heat the upper dust layer while cooling the bottom of the dust layer over East Asia.

Aerosol composition, concentration, and optical and physical properties are important in constraining the radiative effect of aerosols [29–34]. For example, Déandreis used a chemistry–aerosol model and found that the sulfate aerosol direct radiative effect increases almost linearly as the aerosol concentration increases [29]. The aerosol radiative forcing at the bottom and the top of the atmosphere over China were obtained based on the long-term observations within SONET [30]. It is determined that the aerosol radiative forcing at the top of the atmosphere and the surface both doubled during an aerosol event with a peak AOD of 0.6 in Central Europe [31]. The mean atmospheric aerosol radiative forcing of the fine-size absorbing aerosols is found to be much larger than those of coarse dust aerosols and the non-absorbing aerosols during pollution days in Beijing [20]. The composition of aerosols was also found to affect the aerosol radiative forcing efficiency (ARFE) [32].

Compared with the other regions of the world, studies on the aerosol classification over East and South Asia are relatively limited. In this study, 2-dimensional and multi-dimensional methods are used and compared over East and South Asia. We aim at providing a comprehensive characterization of aerosol types, their optical properties, and radiative forcing in East and South Asia. Section 2 describes the data and method

used for this study. The results are shown in Section 3 and discussed in Section 4, and the conclusions are summarized in Section 5.

2. Data and Methods

2.1. Data

AERONET is a federation of ground-based aerosol networks which provides globally distributed retrievals of spectral AOD and aerosol inversion products. Aerosol data are processed at 3 levels of data quality: Level 1.0 (unscreened), Level 1.5 (cloud-screened), and Level 2.0 (cloud-screened and quality-assured) [14]. In this study, the Version 3.0 Level 2.0 daily products of direct sun and inversion (almucantar) algorithm at various channels from 137 sites over the Asian region (10°N–50°N, 70°E–135°E) from March 1998 to February 2018 are used. The AERONET inversion products used include the single scattering albedo (SSA) at the wavelength of 440 nm, extinction Angstrom exponent (EAE), absorption Angstrom exponent (AAE), real refractive index (RRI) and imaginary refractive index (IRI) at the wavelength of 440 nm, aerosol radiative forcing at the top of the atmosphere (ARF_{TOA}), aerosol radiative forcing at the bottom of the atmosphere (ARF_{BOA}), aerosol radiative forcing efficiency at the TOA (ARFE_{TOA}), and aerosol radiative forcing efficiency at the BOA (ARFE_{BOA}). The EAE is calculated with the AOD at the wavelengths of 870 and 440 nm as follows:

$$EAE = -\frac{\log(AOD_{870}) - \log(AOD_{440})}{\log(870) - \log(440)} \quad (1)$$

where large values of EAE (>0.8) typically indicate fine-mode aerosol particles while small values indicate coarse-mode particles.

The AAE is defined similarly as the EAE but using the absorption aerosol optical depth (AAOD) at the wavelengths of 870 and 440 nm:

$$AAE = -\frac{\log(AAOD_{870}) - \log(AAOD_{440})}{\log(870) - \log(440)} \quad (2)$$

The ARF is defined as:

$$ARF_{TOA} = F_{0TOA}^{\uparrow} - F_{TOA}^{\uparrow} \quad (3)$$

$$ARF_{BOA} = F_{BOA}^{\downarrow} - F_{0BOA}^{\downarrow} \quad (4)$$

where F_{0TOA}^{\uparrow} and F_{0BOA}^{\downarrow} represent upward and downward radiative fluxes at the TOA and BOA without aerosol, respectively. The ARFE which denotes the ARF of unit AOD is calculated as:

$$ARFE = ARF / AOD_{550nm} \quad (5)$$

where AOD_{550nm} is the aerosol optical depth at the wavelength of 550 nm.

It should be noted that only limited sites have sufficient valid data for analysis. A valid daily aerosol data sample requires a complete set of the five parameters (SSA, EAE, RRI, AAE, and IRI) without any missing values. It is important to be aware that AERONET inversion data have some inherent limitations. For example, accurate complex refractive index and SSA are only available for the cases with AOD larger than 0.4 under totally clear-sky conditions [33]. In addition, the selected AERONET sites should contain more than 50 valid data samples during 1998–2018. As a result, there are 60 out of 137 AERONET sites that meet the criteria.

The Terra and Aqua satellite combined moderate resolution imaging spectroradiometer land cover climate modeling grid (MCD12C1) Version 6 data product [35] for the year 2017 is used to provide a complete view of land cover and land use over the study region. As very little changes in land cover are observed from 2003 to 2017, we think it is appropriate to use the 2017 land cover.

Monthly means of daily mean meteorological variables including temperature (T), relative humidity (RH), total cloud cover (TCC), and u and v components of wind speed (U and V) from March 1998 to February 2018 are derived from the European Centre for Medium-Range Weather Forecasts Interim Reanalysis (ERA Interim) at the horizontal resolution of $0.125^\circ \times 0.125^\circ$ [36]. Daily precipitation (PR) data is derived from the Tropical Rainfall Measuring Mission (TRMM) Multi-satellite Precipitation Analysis (TMPA) 3B42 Daily Version 7 data set [37] at the latitude range of 50°N – 50°S with a spatial resolution of $0.25^\circ \times 0.25^\circ$. The meteorological variables are re-gridded to the same horizontal resolution of $0.25^\circ \times 0.25^\circ$ to facilitate further analysis.

2.2. Clustering Method to Distinguish Meteorological States

The agglomerative hierarchical clustering algorithm [38] which is a bottom-up and unsupervised learning approach is used to divide different sub-regions with distinct features according to the various meteorological factors in this study. For unsupervised learning, the algorithm is designed to learn the features of the data set without any a priori information or target. Agglomerative algorithm starts with the assumption that each sample in the dataset is an individual and initial cluster (i.e., a grid point having various parameters is regarded as a sample). At the agglomeration step of the algorithm, the two closest clusters are found and merged, and this process is repeated until the desired number of clusters is reached. Here, the hierarchical clustering method is used to identify the meteorological features and to divide regions with similar meteorological conditions (which is referred to as meteorological state, abbreviated as MS in this study). The silhouette coefficient [39] is used to determine the optimal number of clusters. The process of agglomerative hierarchical clustering algorithm and the use of silhouette coefficient are explained in more detail in Appendix A. Figure 1 shows the identification of the optimal partition by the hierarchical clustering algorithm using silhouette coefficient for the data set. It is found that the silhouette coefficients are higher when the numbers of MS are 1, 3, 9, and 12. The result with 3 MS types is considered insufficient to distinguish the climatological features of various regions. However, when the number of MS is 12, the major climatological features are too difficult to be identified and distinguished. Thus, it is deemed more reasonable to choose 9 MS types.

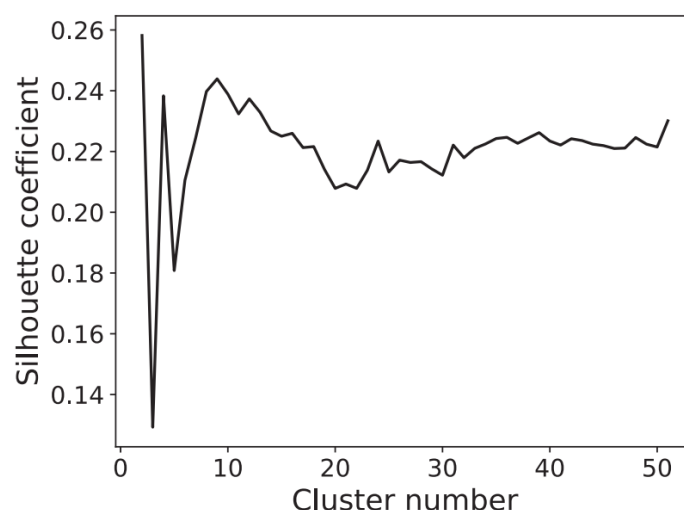


Figure 1. Identification of optimal number of meteorological states using silhouette coefficient with the hierarchical clustering algorithm.

2.3. Clustering Methods to Distinguish Aerosol Types

This section briefly describes the methods and the thresholds to distinguish aerosol types including the 2-dimensional (2-D) clustering methods using three combinations

of aerosol properties and the multi-dimensional Mahalanobis distance (MD) clustering method considering multiple aerosol properties.

2.3.1. The 2-D Clustering Method

In this study, the thresholds for the 2-D clustering method are derived from Bibi et al. [21] who summarized a variety of global clustering approaches for aerosol classification. The thresholds for corresponding methods to distinguish dust, biomass-burning (BB), and urban/industrial (U/I) aerosols are listed in Table 1.

Table 1. The threshold values of various parameters to distinguish the aerosol types.

Aerosol Types	Thresholds					
	SSA and EAE		RRI and EAE		AAE and EAE	
	SSA	EAE	RRI	EAE	AAE	EAE
U/I	0.89–0.96	0.90–1.70	1.35–1.43	0.70–1.74	0.60–1.30	0.80–1.60
Dust	0.88–0.96	0.10–0.40	1.44–1.59	0.01–0.41	1.00–3.00	0.01–0.40
BB	0.82–0.91	0.90–1.70	1.43–1.57	1.00–1.50	1.10–2.30	0.80–1.70

Figure 2 shows a schematic diagram of the 2-D clustering approaches explaining how the aerosol types are determined. The sample points that fall into the boxes are regarded as belonging to the corresponding aerosol types of dust, U/I, or BB. As the EAE is an indicator of particle size [22], the dust aerosols with relatively large particle sizes are conveniently separated from the fine-mode aerosols. For BB and U/I aerosol particles that are similarly small in size, they can be separated by AAE, RRI, or SSA which signify their absorbing capabilities [9,33]. Note the data samples that fall within the overlapped boxes (Figure 2a,c) are both counted as U/I or BB aerosols accordingly as well. This is a drawback of the 2-D method since it is confusing that those aerosol types could not be uniquely derived.

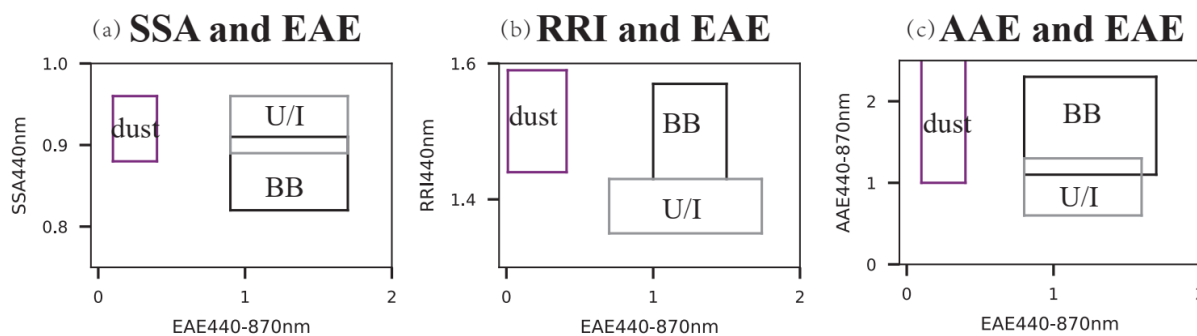


Figure 2. Schematic diagram of the 2-D clustering approaches: (a) using SSA and EAE; (b) using RRI and EAE; (c) using AAE and EAE.

2.3.2. Multi-Dimensional Mahalanobis Distance Clustering Method

A multi-dimensional MD clustering method [40], which considers five aerosol properties (EAE, AAE, SSA, RRI and IRI), is also used to identify the aerosol types. Hamill et al. [17] used the AERONET Level 2.0 almucantar aerosol retrieval products over the world for the period from 1993 to 2012 to define several reference aerosol clusters. The classification of these aerosol types is determined by its 5-dimensional MD for each reference cluster.

The MD is calculated as follows. The values of N parameters at a grid point form an N -dimensional vector \mathbf{a} , which is written as $\mathbf{a} = (a_1, a_2, \dots, a_N)^T$. In our case, N equals to 5 and \mathbf{a} represents the daily aerosol properties which includes 5 parameters (SSA, AAE, EAE, RRI and IRI). The centroid of the five reference clusters (see Table 2) for the

aerosol type (BB, U/I, dust, maritime, and mixed aerosol) [17] is represented by the vector $\mathbf{b} = (b_1, b_2, \dots, b_N)^T$. The covariance matrix \mathbf{C} is defined as

$$\mathbf{C} = \text{cov}(\mathbf{a}, \mathbf{b}) = E[(\mathbf{a} - E[\mathbf{a}])(\mathbf{b} - E[\mathbf{b}])] \quad (6)$$

where E is the mathematical expectation. Then the MD is defined as

$$\text{MD} = \left[(\mathbf{a} - \mathbf{b})^T \mathbf{C}^{-1} (\mathbf{a} - \mathbf{b}) \right]^{\frac{1}{2}} \quad (7)$$

In this study, the values of centroid and distance are derived from Hamill et al. [17] who designed the centroids based on global site analysis. The definition of reference cluster is to keep only points within an MD of 2 from the centroid, which roughly equals to keeping 45% of the samples within the training data set in the process of building the model [17]. Table 2 lists the centroids of five reference parameters for each aerosol type. All the points having an MD larger than 2 from the centroids are discarded and are not considered as any types of aerosols.

Table 2. The centroids of 5 reference parameters of each aerosol type.

Aerosol Type	SSA	EAE	RRI	AAE	IRI
BB	0.89	1.87	1.48	1.3	0.02
U/I	0.96	1.76	1.4	1.15	0.005
Dust	0.91	0.28	1.47	1.75	0.004
Mixed	0.92	1.32	1.45	1.2	0.011
Marine	0.97	0.59	1.4	0.93	0.001

3. Results

3.1. Land Cover and Meteorological States

The study area (10°N~50°N, 70°E~135°E) includes East and South Asia with various land cover and meteorological conditions. A hierarchical clustering method is used to divide sub-regions to facilitate detailed discussions.

The land cover in the study area contains 17 kinds of land use (Figure 3). Certain areas have very distinctive land use as compared with the other regions. For example, the northern part of India, east and northeast China, and the central part of the Indo-China Peninsula (IP) are mostly farmland. In the northern part of IP, southern China, and Taiwan, the land cover is mainly forest, shrub, and farmland. In the southeast of the Tibetan Plateau (TP) and Inner Mongolia Plateau, most of the vegetation is grassland. The northern part of the TP and the Tarim Basin are basically bare land without vegetation. Industrial and urban landscapes are mostly located near densely populated cities. Note: it is deemed reasonable to use the land cover of the year 2017 for analysis, since only 4 out of 60 AERONET sites experienced land cover changes from 2003 to 2017. For the AERONET sites used in this study, about half (30) of the sites were located near major cities, and the rest mostly have land cover of forest or grassland.

Previous studies showed that certain aerosol types are closely related to the characteristic land cover in particular regions. For example, bare lands and grasslands in northwest Asia were considered as the major sources of dust aerosols [2]. Agricultural activities and forest fires could produce aerosols due to biomass combustion [41]. In densely populated areas, garbage combustion, traffic exhaust, and fossil fuel combustion could bring about urban pollution [3,5].

The meteorological conditions are also important factors to determine the aerosol type over certain regions. The nine meteorological states from the hierarchical clustering process considering six meteorological factors (T, PR, RH, TCC, U and V at 1000 hPa) in the South and East Asian region are shown in Figure 4 wherein a large-scale perspective of the climatological feature is provided. Table 3 shows the regional annual average and variance of the meteorological conditions in the nine MS areas.

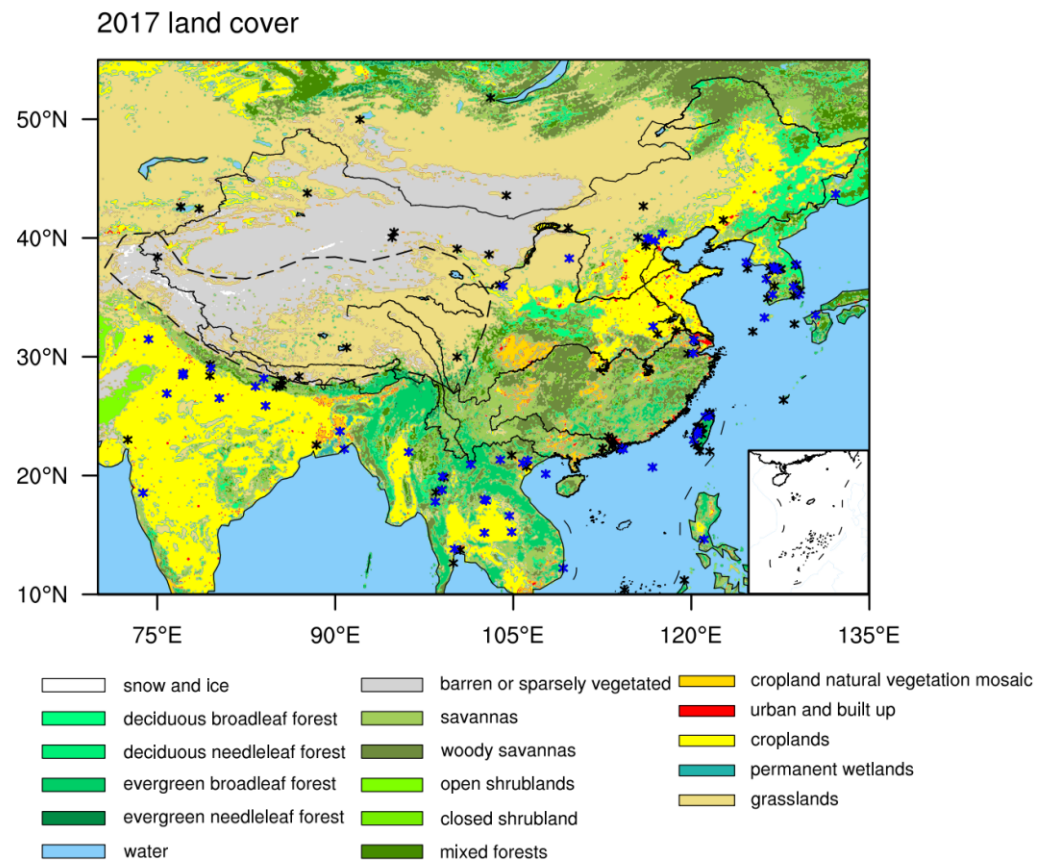


Figure 3. The distributions of land cover in East and South Asia in 2017. The asterisks represent the locations of AERONET sites with the blue asterisks indicating the 60 sites having enough valid data for analysis. The dash line is the contour of altitude of 3000 m.

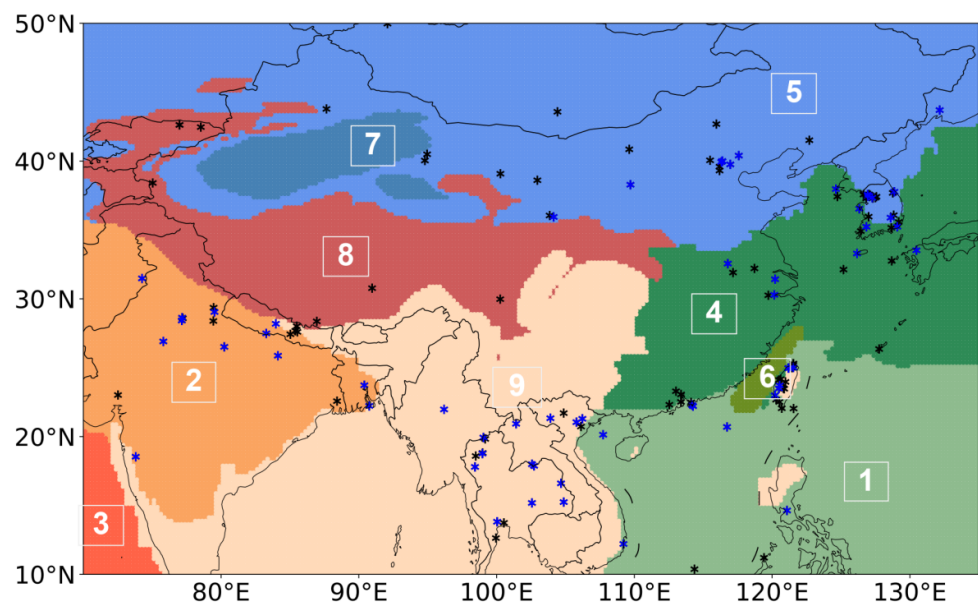


Figure 4. The nine meteorological states identified with the hierarchical clustering algorithm are highlighted with different colors. The asterisks indicate the locations of the AERONET sites with the blue ones showing the sites with enough valid data for analysis.

Table 3. The annual average and variance of the meteorological variables in nine MS areas.

	MS 1	MS 2	MS 3	MS 4	MS 5	MS 6	MS 7	MS 8	MS 9
T (°C)	25.6	28.2	26.7	17.3	12.7	21.3	20.5	21.2	25.8
PR (mm/d)	5.6	2.7	4	4.2	1	4.2	0.2	1.2	5.2
U (m/s)	−3	0.6	3	−0.2	0.9	−2.9	−1.1	1.2	0.4
V (m/s)	−1	−0.1	−2.2	−1.1	−0.3	−3.3	−1.2	0.5	0.5
RH (%)	78.9	59.3	75.1	73.7	55.6	81.2	31.1	60.3	78.1
TCC (%)	60.8	31.4	45	55.4	42.7	49.7	36.2	53.5	58.9
σ^2 (T)	1.7	2.2	0	13.2	22.5	1.9	3	4.2	4.8
σ^2 (PR)	2.2	1.6	2	1.4	0.5	0.4	0	0.4	4.4
σ^2 (U)	1.4	0.4	0	1.1	0.8	0.3	1.1	1	0.7
σ^2 (V)	0.3	0.2	0.1	0.5	0.4	0.3	0.3	0.4	0.4
σ^2 (RH)	1.8	59.3	3	11.4	128.7	1.7	23.7	99.8	17.4
σ^2 (TCC)	69.3	81.7	88.2	10.9	43.7	21.8	8.1	38.4	73.8

It is apparent that each MS has some unique features. For example, the MS 5 and MS 7 areas are located in the mid-latitude region where westerly winds are dominant in spring, autumn, and winter (Figure S4). The MS 7 area is basically bare land without vegetation (Figure 3) where the PR (0.2 mm/d) and RH (31.1%) are the lowest among all the MS areas (Table 3). In the MS 5 area, the land use changes from bare land and grassland in the west to cropland and urban cities near Bohai Bay. In spring, the MS 5 area is mostly affected by the dry northwest wind that brings a lot of dust [2,10].

The MS 2, 3, and 9 areas are overall affected by the south Asian monsoon system [42], but they also show some differences. Southwest wind prevails in spring and summer at the MS 2 and MS 9 areas. The prevailing westerly winds in spring and summer bring dust aerosols from the Arabian Peninsula and the Thar Desert to MS 2 [26,43]. The MS 9 area includes the Bay of Bengal, IP, central Nepal and the coastline of the Indian Peninsula (Pune site). The PR in the MS 9 area (5.2 mm/d) is significantly higher than that (2.7 mm/d) in the MS 2 area (see Table 3). Higher precipitation may be the key reason for the lack of AERONET data in summer over IP. The MS in East Nepal (Pokhara site) are very different from those in the Indian peninsula (Figure 4), and topographic barrier is considered as the reason for the high precipitation located around Pokhara [44].

In winter, north wind prevails and brings the aerosols from northern and northwestern China to the MS 4 area [25]. In summer, the MS 1, 4, and 6 areas are affected by the southwest monsoon which bring BB aerosols from southeast Asia to the Asian continent [45]. The MS 1 area belongs to the tropical monsoon region and the MS 4 area is located near the subtropical monsoon region [42]. The Tibetan Plateau and its surrounding area constitute the MS 8 which features large variability of RH.

It can be seen from the above analysis that the nine MSs classified by the hierarchical clustering method contain distinctive local climatology features. The next section shows the aerosol types identified by different methods at various sites within the different MSs in East and South Asia.

3.2. Aerosol Classification Using Multi-Dimensional Mahalanobis Distance Method

A multi-dimensional MD method accounting for all five available aerosol parameters is used to classify the aerosol types within different regions. For the convenience of analysis and discussion, several sub-regions (see Table 4) are divided based on the MS (Figure 4) and the distances as discussed in the Section 3.1.

Figure 5 shows the percentages of five different types of aerosols (namely BB, U/I, dust, mixed, and marine aerosols) identified through the MD method in various sub-regions. It is evident that a large portion of aerosol is undetermined. The percentages of identified aerosol types as well as the undetermined ones vary remarkably in different sub-regions and seasons. Dust aerosols are dominant in summer in the NIGP area (34%) and in spring at the SACOL site (37%). The proportions of U/I aerosols in the Beijing area (15%), Hong

Kong area (18%), Yangtze River Delta (24%), CIP area (18%), Hanoi area (10%), Taiwan area (25%), and Korea and Japan area (29%) are the largest in summer. A large amount of BB aerosols is identified in the CIP area especially in spring (35%) and winter (12%). Located at an agricultural and animal husbandry economic zone, the Ussuriysk site shows 24% of BB aerosols in spring which is attributed to vehicle transportation pollution and forest and agricultural vegetation fire [41,46]. Note that a large number of aerosols are identified as mixed aerosol type. This could be partially attributed to the way how the MD method classifies aerosols through establishing a representative training data set by using global observations. A previous detailed examination shows that the U/I aerosols in some cities in Asia are classified into mixed type, as they tend to be far from the centroids of the major aerosol types [17].

Table 4. The AERONET sites within the divided sub-regions.

Sub-Region	AERONET Sites
NIGP area	New_Delhi, Gual_Pahari, Lahore, Pantnagar, Kanpur, Gandhi_College, Jaipur
Central Nepal area	Pokhara, Lumbini
Bangladesh area	Dhaka_University, Bhola
CIP area	Chiang_Mai_Met_Sta, Doi_Ang_Khang, Omkoi, Son_La, Luang_Namtha, Nong_Khai, Vientiane, Pimai, Mukdahan, Silpakorn_Univ, Ubon_Ratchathani, NhaTrang
Hanoi area	NGHIA_DO, Bac_Giang, Bach_Long_Vy
Hong Kong area	Hong_Kong_PolyU, Hong_Kong_Hok_Tsui
Taiwan area	Taipei_CWB, EPA-NCU, NCU_Taiwan, Chiayi, Douliu, Chen-Kung_Univ
Yangtze River Delta	Taihu, Hangzhou_City, Shouxian
Korea and Japan area	Baengnyeong, Seoul_SNU, Yonsei_University, Hankuk_UFS, Anmyon, Gwangju_GIST, Gosan_SNU, Gangneung_WNU, KORUS_Kyungpook_NU, Pusan_NU, Fukuoka
Beijing area	Beijing_RADI, Beijing, Beijing-CAMS, XiangHe, Xinglong
Single sites	SACOL, Yulin, Ussuriysk, Pune, Dongsha_Island, Manila_Observatory, Mandalay_MTU

It is interesting to find that our aerosol classification results only show limited fractions of pure marine aerosols even at the coastal sites near Bohai Bay, Yangtze River Delta, Taiwan, and Hong Kong. This is contrary to the previous results at the coastal sites over the world where marine aerosols are predominant in different seasons [47,48]. Some occurrences of BB aerosol are found over the Yangtze River Delta which are similar to those in the Baikal region [49] but in a different season (winter). We also found much higher percentages of mixed aerosols but lower percentages of U/I aerosols than those at the other coastal sites [50,51]. This is mostly attributed to the use of different classification methods.

We further show the results of aerosol classification by using 2-D methods with three sets of combinations of parameters and thresholds in the next section. Since no other reliable aerosol type information is available, we treat the aerosol types identified through the MD method as the “correct” results to be compared with.

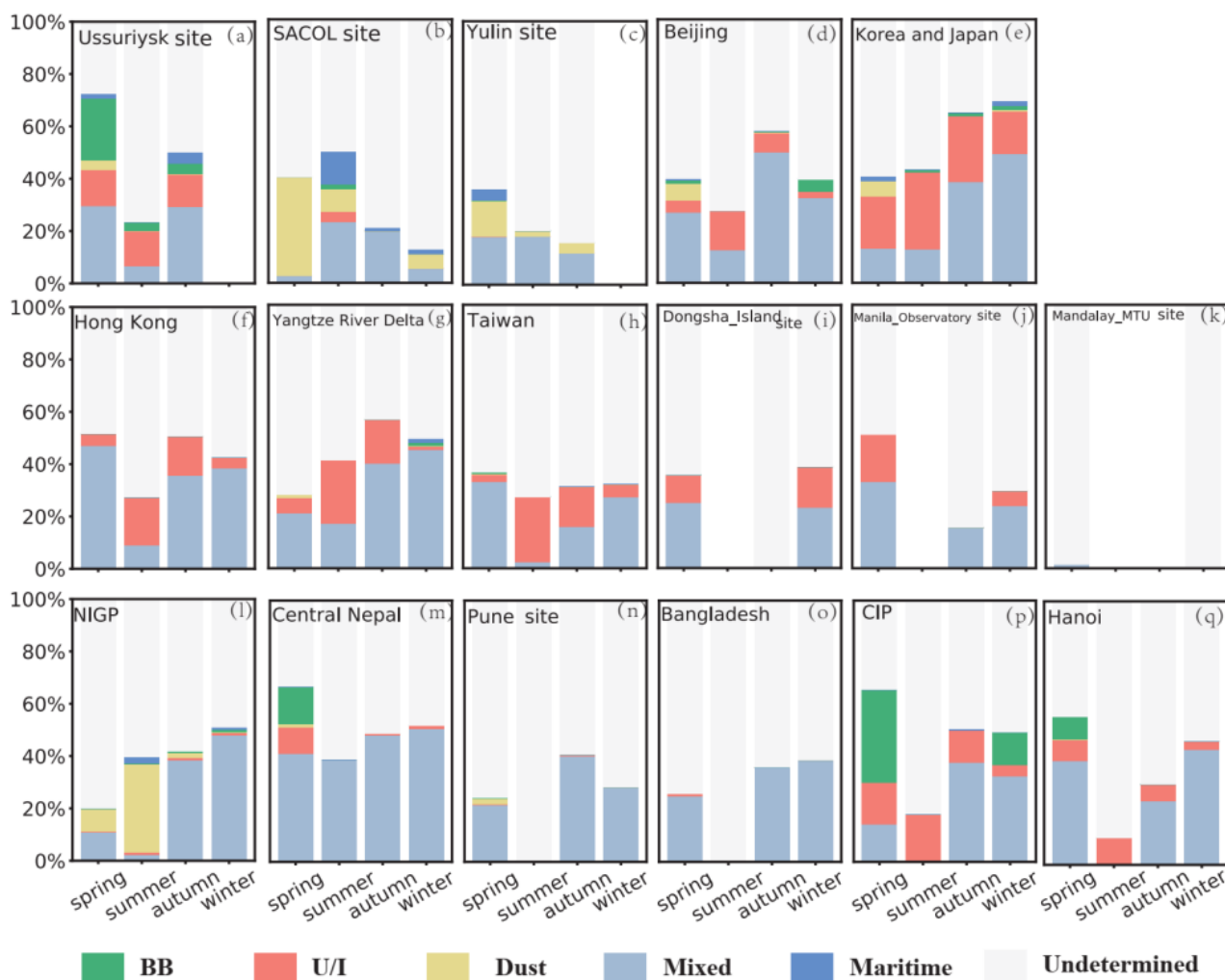


Figure 5. The percentages of different types of aerosols in various sub-regions identified through the MD method.

3.3. Aerosol Characteristics Identified by the 2-D Methods

The discrimination of aerosol types by applying the 2-D aerosol classification methods using different combinations of aerosol parameters (AAE and EAE, SSA and EAE, and RRI and EAE) at different sub-regions are shown in Figures 6–8. Note that each method shows certain advantages in distinguishing aerosols which are to be elaborated below.

3.3.1. The 2-D Aerosol Classification Using AAE and EAE

Figure 6 shows the clustering results for the sites in South Asia using the 2-D AAE-EAE method. The boxes drawn in each subplot correspond to the thresholds listed in Table 1 (Figure 2c). At the two sites (Lumbini and Pokhara, Figure 6a,b) in central Nepal, U/I aerosols are dominant in summer and BB aerosols are dominant in autumn and winter. The pollution sources are mainly local forest fire, fossil fuel combustion, crop residue burning, and the aerosols transported from the Northern Indo-Gangetic Plain (NIGP) area to Nepal [52,53]. Although Nepal (Figure 6a,b) is close to northern India, their aerosol classification results are different. In northern India, dust aerosols (Figure 6c–i) mainly exist in spring and summer and come from Thar Desert, Afghanistan/Iran, and the Middle-Eastern Peninsula to the MS 2 area (Figure 4) by the prevailing westerly winds [26,43]. The proportion of dust aerosols in summer are higher than that in spring. In the seven sites near northern India (Figure 6c–i), there is a significant negative correlation between EAE and AAE in spring and summer (passed the 95% confidence level) when $EAE < 0.8$. The

EAE values of sites in northern India are overall lower than those in other sites over the whole study region. For example, the averaged value of EAE at the Jaipur site (Figure 6e) in summer is 0.4 which is the lowest among all sites.

The comparisons with the MD results show that the results from the 2-D AAE-EAE method contain much less undetermined aerosols and much higher proportions of U/I and BB aerosols. However, we could see that a large portion of aerosols with AAE values around 1 are actually hardly distinguishable. Similar features can be found in the Bangladesh and Hanoi areas in Figure S2 with the exception of the CIP area where the EAE of aerosol is excessively high and which even surpasses the upper limits of the threshold for 2-D aerosol classification.

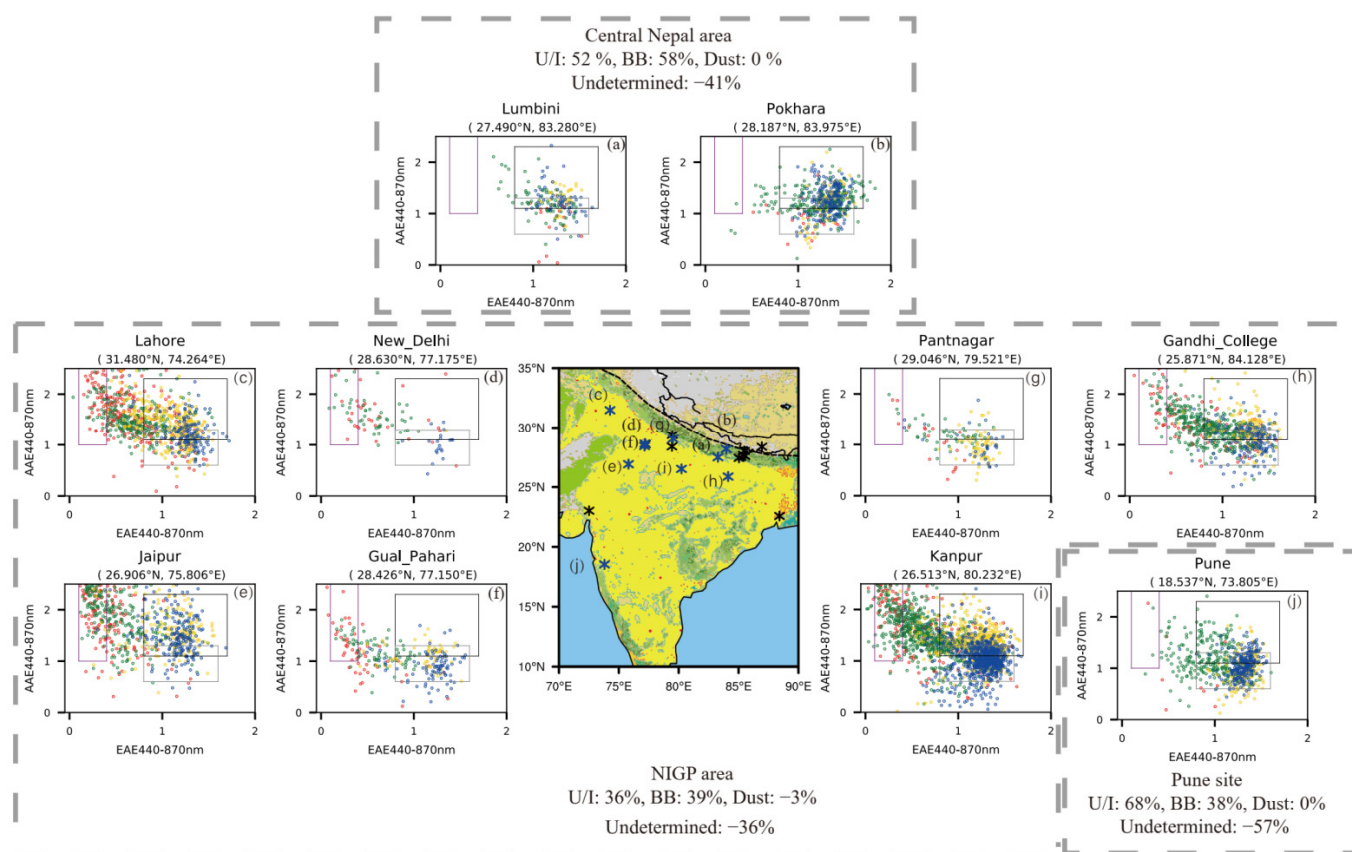


Figure 6. The aerosol types at the AERONET sites (a–j) near India identified by the 2-D clustering method using AAE and EAE for the period of March 1998 to February 2018. The blue asterisks on the map indicate the locations of the sites with enough valid data for analysis, while the black ones represent the sites that are not used. The green, red, yellow, and blue dots on the scatter plots represent the data in boreal spring (March, April, and May), summer (June, July, and August), autumn (September, October, and November), and winter (December, January, and February), respectively. The boxes plotted with dashed lines indicate the sub-regions listed in Table 4. For each sub-region, the differences in percentage (2-D result minus MD result) for the U/I, BB, dust, and undetermined aerosols are shown, respectively.

3.3.2. The 2-D Aerosol Classification Using SSA and EAE

Figure 7 shows the aerosol clustering results at various sites in northern China using SSA and EAE as inputs to the 2-D classification method. The boxes drawn in each subplot correspond to the thresholds listed in Table 1 (Figure 2a). All the sites in Figure 7 belong to the MS 5 area. The northwest wind brings dust from the Taklimakan Desert, Inner Mongolia, and Mongolia arid regions (MS 7) to the MS 5 area [54]. At the SACOL site (Figure 7a), it is apparent to find dust aerosols in all seasons with the largest rate of occurrences in spring

(30%), and the U/I aerosols prevail in the other seasons. It is found that quite a few data samples with medium sizes are un-classified as either dust or fine-mode aerosols in every season. The Yulin site shows much lower SSA value because of the black carbon emission from nearby enterprises that produce coal, chemical, oil, and gas [55].

For the several sites near the Beijing metropolitan region (Figure 7c–g), the U/I aerosols are dominant in summer and autumn. It is found that the averaged SSA in this area is especially high in summer (0.94). This could be due to the impacts of aerosol hygroscopic growth as Xia et al. found that there is a clear positive relationship between relative humidity and the SSA [23]. Similar to the previous studies, we find the proportions of BB aerosols in winter are higher than those in autumn and summer [56–58], which is related to the local residential biofuel use, such as crop residuals and softwood burning [8,59]. The Xinglong site, which is located at the rural and mountainous area, is far from the source of BB aerosols and thus exhibits much higher SSA values [60]. Dust aerosols also exist in spring at the five sites near Beijing which could be originating from arid regions in Inner Mongolia and Mongolia [8].

It is observed that the 2-D SSA-EAE method is relatively effective in identifying dust aerosols which agrees well with the results from the MD method at the SACOL site, Yulin Site, and Beijing area. However, there is still a 30–40% difference in U/I aerosols and 20–30% difference in BB aerosols. The differences in the percentage of undetermined aerosol between the 2-D SSA-EAE and the MD methods reduce to 11% in the Korea and Japan area (Figure S3).

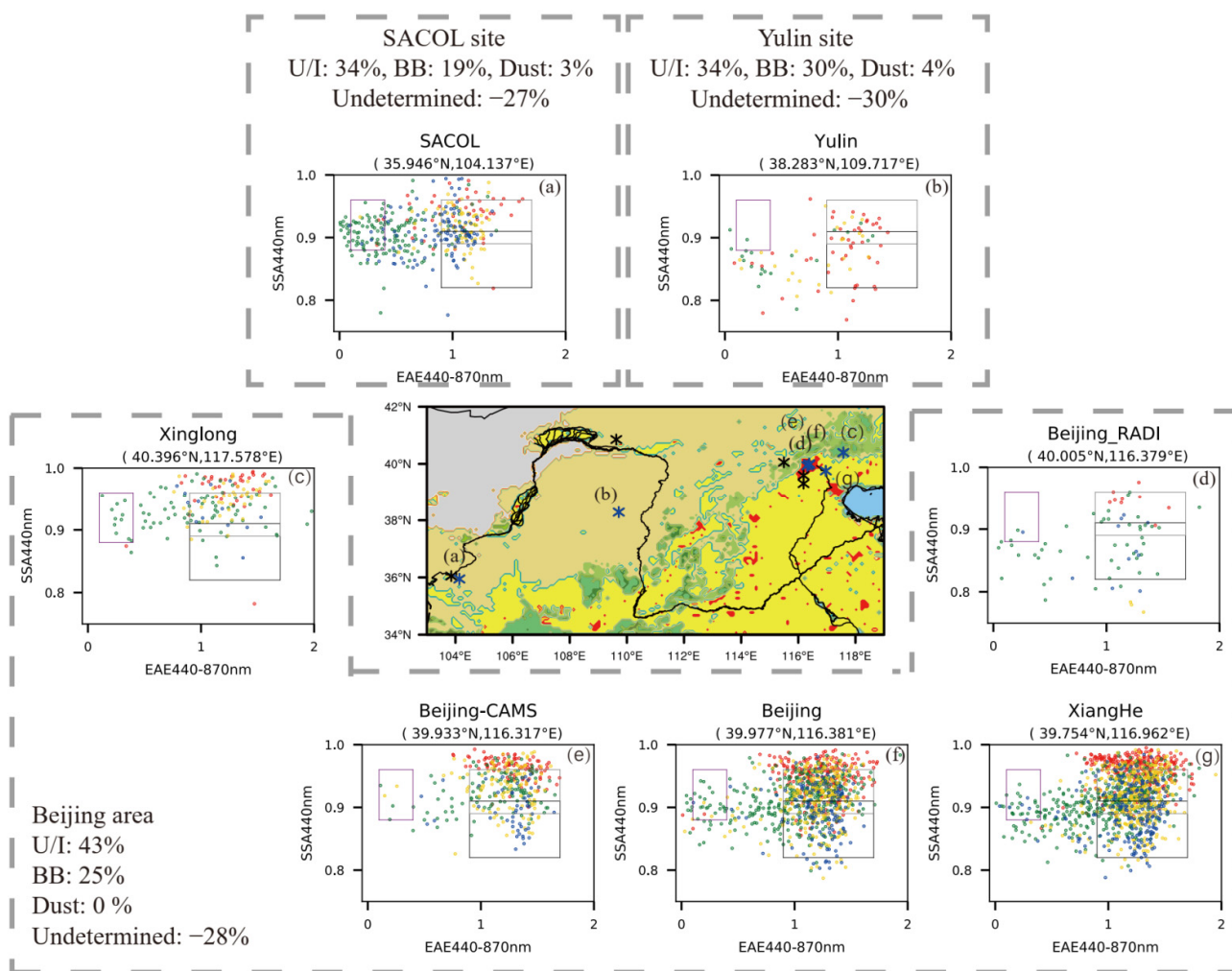


Figure 7. The same as Figure 6 but for the aerosol classification by the 2-D clustering method using SSA and EAE at the AERONET sites (a–g) in northern China.

3.3.3. The 2-D Aerosol Classification Using RRI and EAE

Overall, it is found that the SSA values in East Asia are higher than those in South Asia. For example, among the 11 sites in Japan and Korea (Figure S3a–c,e–l), the averaged values of SSA range from 0.93 to 0.96 as compared with those in northern India ranging from 0.87 to 0.9. The aerosols at the sites in the Taiwan area typically have high SSA values of over 0.9. The Chen-Kung_ Univ site in summer even has the highest SSA (0.99) in the whole area. The 2-D classification method using SSA and EAE is somewhat limited in distinguishing aerosols with similarly high SSA parameters in such regions. Comparatively, the averaged RRI values of sites in Taiwan (1.38–1.43) are lower compared with other sites in East and South Asia. For instance, the averaged value of RRI in Douliu site (1.4) is the lowest in the whole study area. Considering the excessively high and densely distributed SSA, the 2-D aerosol classification method using RRI and EAE is selected for this sub-region.

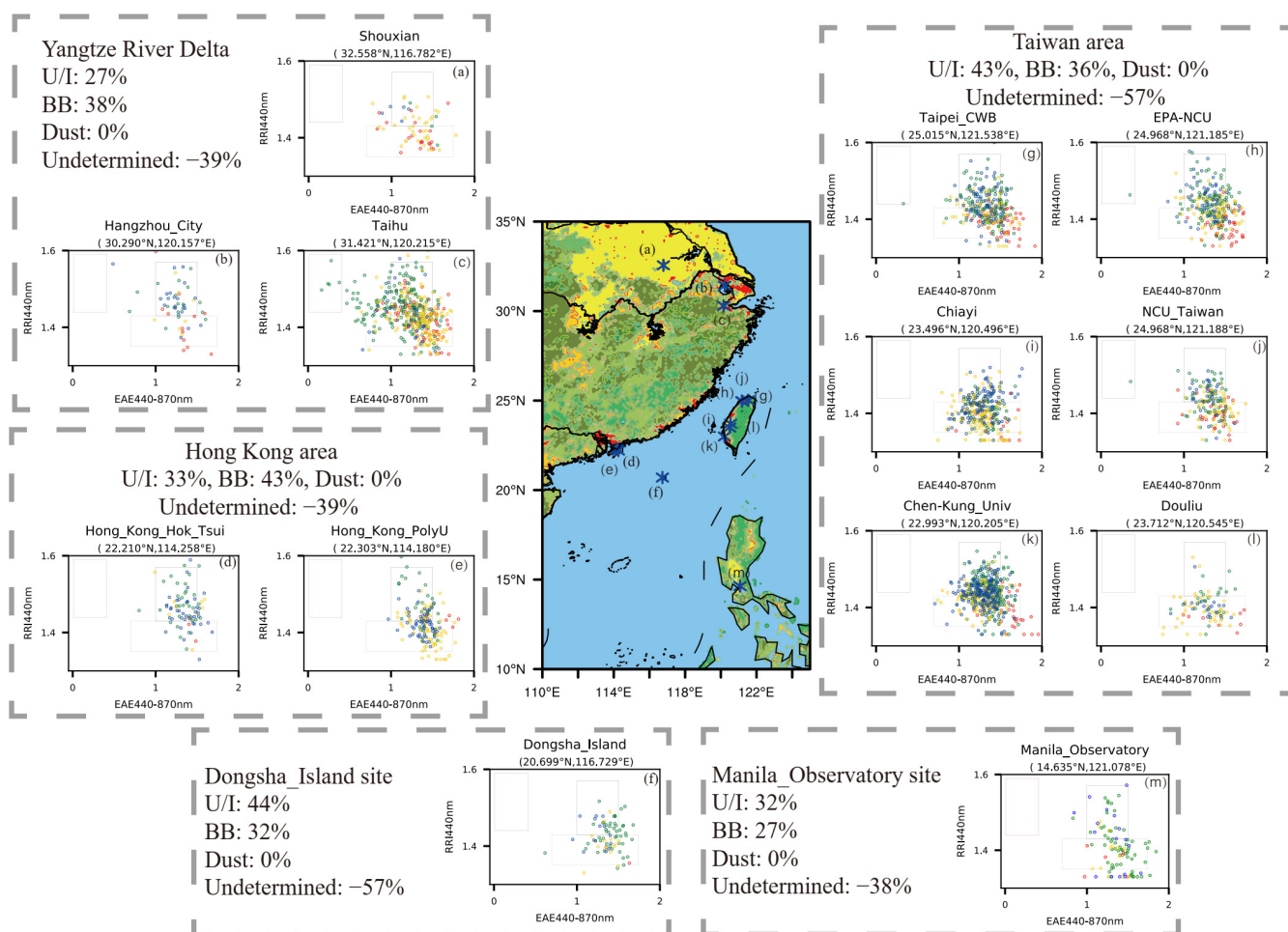


Figure 8. The same as Figure 6 but for the aerosol classification by the 2-D clustering method using RRI and EAE at the AERONET sites (a–m) in Southeast Asia.

Figure 8 shows the results of aerosol classification in southeast Asia using the 2-D method with RRI and EAE. The boxes drawn in each subplot correspond to the thresholds listed in Table 1 (Figure 2b). It is found that the BB and U/I aerosols are the major aerosol types within this sub-region. The U/I aerosols in summer and autumn are dominant in Shouxian site (Figure 8a), Taihu site (Figure 8c), and Taiwan area (Figure 8g–l). The proportion of BB aerosols in Taiwan in spring ranges from 23% to 54%, which is largely affected by the BB aerosols transported from IP region as is elaborated in some previous studies [3,61]. There is basically no local emission from biomass combustion in Hong Kong, thus the source of BB aerosols is also attributed to the long-range transport from

the Indochina Peninsula and Philippines [62,63]. Among the sites shown in Figure 8, the averaged EAE value at the Yangtze River Delta sites is lowest, especially at the Taihu site during spring. The result in the Taihu site (Figure 8c) shows sporadic dust aerosols in spring, which is related to the impacts of aerosol long-distance transport from the northwest of China [64].

Large discrepancies are evident between the results from the 2-D RRI-EAE and the MD methods. The majority of the data samples fall within the thresholds for 2-D classification, which results in much higher proportions of U/I and BB aerosols and much lower proportions of undetermined aerosols as compared with the MD method. However, the seemingly acceptable performance of the 2-D RRI-EAE method actually deviates from the results of the MD method.

This section shows the aerosol types classified by the 2-D classification approach using three sets of aerosol properties (namely SSA and EAE, AAE and EAE, and RRI and EAE) over East and South Asia. On the one hand, the three classification methods perform similarly well in identifying the major aerosol types. On the other hand, the proportions of different aerosol types classified by various methods are different. For example, the proportions of BB aerosol classified using the 2-D RRI-EAE and the 2-D AAE-EAE methods are much higher than those using the 2-D SSA-EAE method in the area around Japan and Korea. Previous studies confirmed that the 2-D approaches using AAE or RRI could overestimate the proportion of BB aerosol in Japan and South Korea [65,66]. It is considered that the 2-D clustering method is handy for identifying the major aerosol types, but the results of aerosol proportions are highly dependent on the specific aerosol parameters as well as the thresholds used for identification which is of critical importance. More discussions of the results from the 2-D methods and the MD method are addressed in Section 4.

3.4. Aerosol Radiative Forcing and Radiative Forcing Efficiencies of Various Aerosol Types

In this section, the ARF and ARFE of each aerosol type in various sub-regions are quantified. The ARF and ARFE are negative at the BOA and the TOA, which means that aerosols exert a cooling effect [1]. It is also noted that the ARF and ARFE at the BOA are stronger than those at the TOA. We focus on the ARF and ARFE of various aerosol types classified by the MD method, and the results from the 2-D methods are shown in the Supplementary Materials (Figures S4–S7). Note the name “undetermined aerosol” refers to (1) the samples that are not classified as either dust, U/I, BB, marine, or mixed aerosols in the MD case, and (2) the samples that are not classified as either dust, U/I, or BB in the 2-D case.

Figure 9 shows the daily averaged ARF_{TOA} of various aerosol types classified with the MD method in different regions. The ARF_{TOA} values vary from -51 to -31 W/m^2 for dust aerosols, -50 to -22 W/m^2 for U/I aerosols, -51 to -15 W/m^2 for BB aerosols, -85 to -21 W/m^2 for marine aerosols, -54 to -23 W/m^2 for mixed aerosols, and -53 to -21 W/m^2 for undetermined aerosols. Apart from the undetermined aerosols, it is evident that dust and marine aerosols almost always contribute the most to the daily averaged ARF_{TOA} whenever they are present, followed by U/I and BB aerosols. It is also noticed that the daily averaged ARF_{TOA} of mixed and undetermined aerosols are similar in magnitude, and they both vary greatly with sub-regions with particularly strong influence occurring around large cities where the AOD value of the undetermined aerosol is high, like Beijing and Shanghai. The characteristics of the daily averaged ARF_{BOA} mostly resemble to those of the ARF_{TOA} except that the values are about doubled for U/I, dust, and marine aerosols, about tripled for BB aerosol, and about 2 to 3 times for mixed and undetermined types (Figure 10). These features are closely related to the unique properties of individual aerosol types.

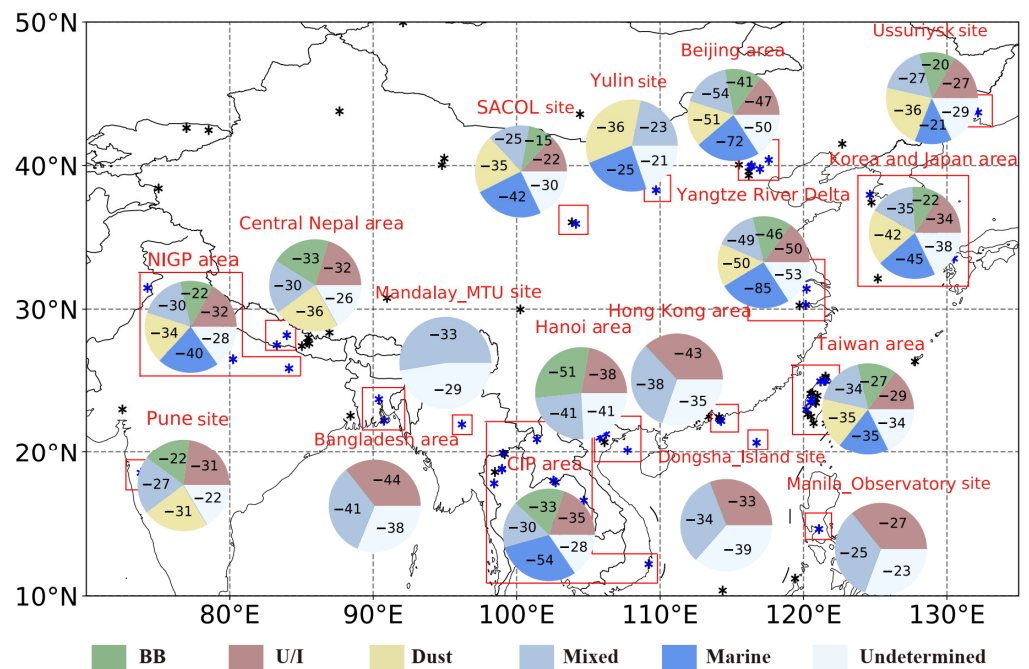


Figure 9. The daily averaged ARF_{TOA} for various aerosol types based on the MD classification method. The numbers in the pie chart indicate the averaged ARF of the corresponding aerosol type (Unit: W/m^2). The blue asterisks on the map indicate the locations of the sites used for analysis, while the black ones represent the sites that are not used.

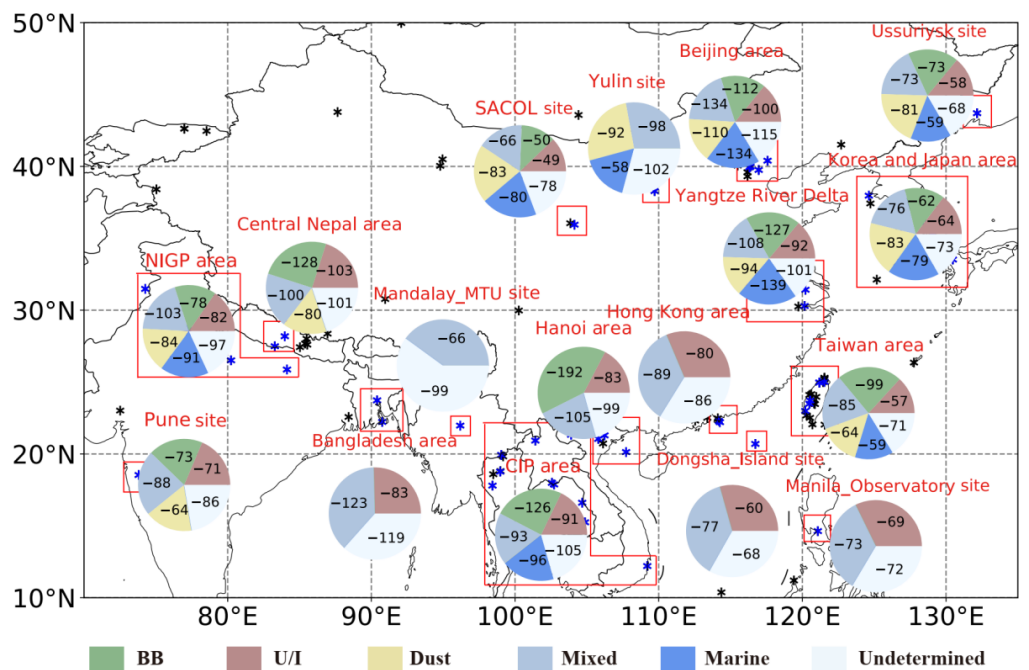


Figure 10. The same as Figure 9 but for the ARF_{BOA} .

Figure 11 shows the daily averaged $ARFE_{TOA}$ for the aerosol types identified through the MD method in various regions. The $ARFE_{TOA}$ of dust and marine aerosols are among the strongest among all aerosol types. The $ARFE_{TOA}$ of U/I aerosols is stronger than that of BB aerosols, except in the Beijing area. It is interesting to find that the dust $ARFE_{TOA}$ over East Asia is apparently higher than that over South Asia, which could be indicative of the different compositions of dust that lead to different absorbing capabilities. Comparatively, the U/I aerosols could be more influenced by the moisture conditions which are related to

the hygroscopicity of U/I aerosols [67]. We could find noticeable differences in the $ARFE_{TOA}$ of U/I aerosol between continental sites and coastal or marine sites. The $ARFE_{TOA}$ for BB aerosol is somewhat more stable around $40\text{--}60\text{ W/m}^2/\text{AOD}_{550\text{nm}}$. Contrary to the $ARFE_{TOA}$, the $ARFE_{BOA}$ of BB aerosol is the strongest ($-139\text{ to }-198\text{ W/m}^2/\text{AOD}_{550\text{nm}}$) among all types of aerosols (Figure 12). It is also noticed that the $ARFE_{BOA}$ has some seasonal variations. The daily averaged $ARFE_{BOA}$ in summer is the weakest among all seasons (figure not shown), which is likely related to the weakening of ARFE by RH increase. Yoon and Kim [68] reported that although the AOD and ARF both increase as the RH increases, the ARFE ultimately decreases accordingly.

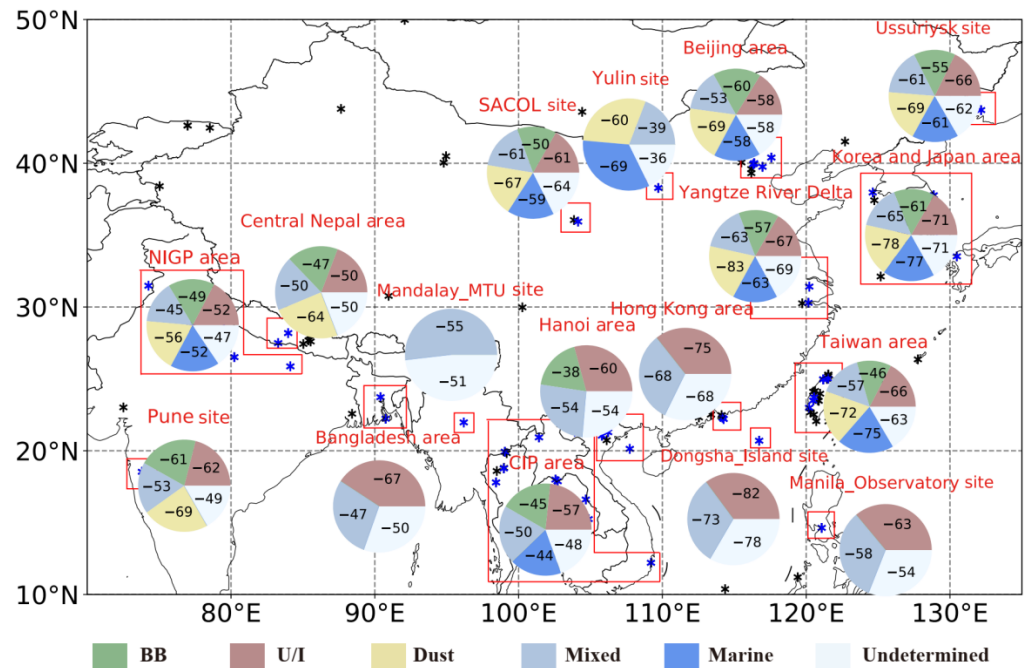


Figure 11. The same as Figure 9 but for the $ARFE_{TOA}$ (Unit: $\text{W/m}^2/\text{AOD}_{550\text{nm}}$).

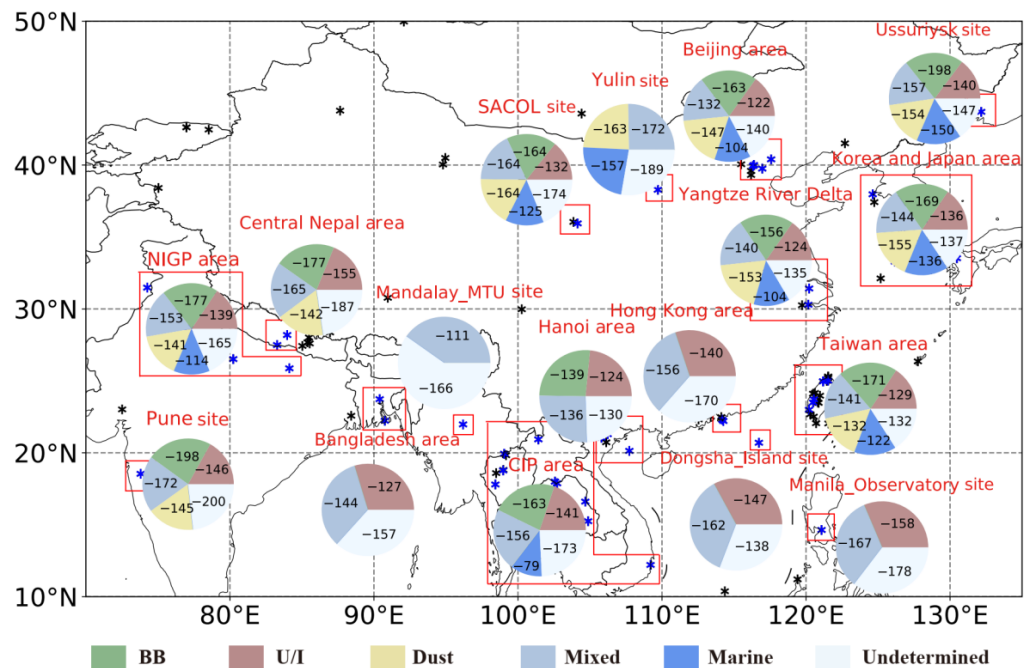


Figure 12. The same as Figure 9 but for the $ARFE_{BOA}$ (Unit: $\text{W/m}^2/\text{AOD}_{550\text{nm}}$).

4. Discussion

This section generally discusses the differences in the proportions of various aerosol types between the MD and the 2-D classification results. The corresponding differences in ARF and ARFE for each aerosol type are also quantified.

4.1. The Differences in the Proportions of Various Aerosol Type Classified by 2-D and MD Methods

We provide a table listing the differences in percentages of individual aerosol types between the 2-D and MD results in Table S1, in addition to the Figures 6–8, Figures S2 and S3. Although the results from the 2-D methods do show some similar features as those from the MD methods, such as the high proportion of BB aerosols during spring in the CIP area and the high proportions of U/I aerosols during summer in the Beijing, Korea–Japan, and Taiwan areas, the 2-D results could be problematic in that they attribute too many un-identifiable aerosol samples to certain known types. Compared with the 2-D method, the MD method with multiple parameters is expected to reduce the uncertainties caused by selected aerosol optical parameters that could be obviously different in local areas.

To better quantify the performances of the 2-D methods, we gather all the data samples in the East and South Asian region that could be classified by the MD method and plot the results from 2-D perspectives in the same way as with the 2-D approaches (Figure 13). Table 5 shows a summary of the percentages of the known aerosol types that could be identified through the 2-D methods (the data samples that fall within the boxes). It is clear that the 2-D methods perform differently for different types of aerosols. The 2-D methods all could identify 43–48% of dust aerosols but uniformly miss the dust aerosols that are relatively smaller in size (with larger EAE). Comparatively, the 2-D methods could not reach a consensus for U/I and BB aerosols. The 2-D RRI-EAE method identifies about 56% of the total U/I aerosols, while the other two methods classify 49.7% and 39.8%, respectively. Even larger discrepancies are found for BB aerosols where the 2-D AAE-EAE method identifies 50% while the 2-D RRI-EAE method only catches 6.3%. It is noted that the 2-D methods are more suitable to be used to identify pure aerosol types than the mixed type.

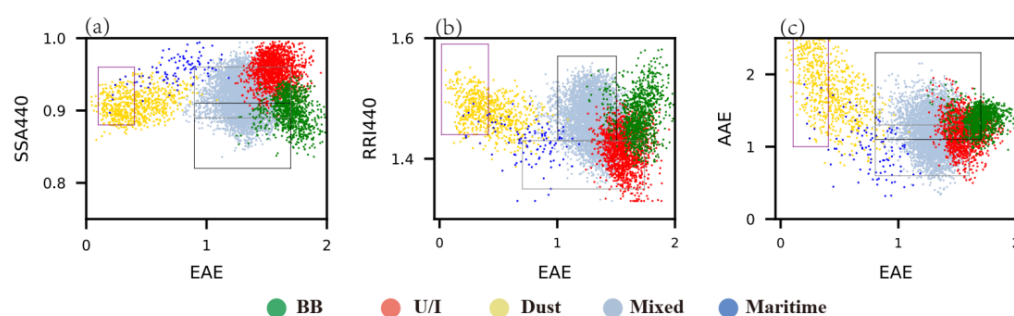


Figure 13. Scatterplots of aerosol samples with known types identified through the MD method in the form of 2-D classification using the parameters and thresholds (the boxes) similar as Figure 2: (a) SSA and EAE; (b) RRI and EAE; (c) AAE and EAE.

Table 5. The percentages of the known aerosol types that could be also identified through the 2-D methods (unit: %).

	U/I	BB	Dust
2-D SSA-EAE	49.7	32.5	43.7
2-D RRI-EAE	56.3	6.3	48.1
2-D AAE-EAE	39.8	50.1	47.7

From the Figure 13, we could also see that the aerosol clusters are barely regular in shape and could have overlaps on 2-D perspectives. As a result, it is highly uncertain

to use the 2-D aerosol classification methods that rely on only two parameters and fixed thresholds.

4.2. The Differences in Aerosol Radiative Forcing and Forcing Efficiency by the 2-D and MD Classification

The ARF and ARFE at the TOA and BOA estimated based on the MD and the 2-D methods using AAE and EAE, RRI and EAE, and SSA and EAE can be derived accordingly (shown in Figures S4–S7 and Tables S2 and S3). The major features of ARF and ARFE identified above still remain. For example, the ARF_{TOA} and $ARFE_{TOA}$ of dust are still the strongest among all aerosol types, and the $ARFE_{BOA}$ of BB aerosols is still larger than that of U/I aerosols. The features including that the dust $ARFE_{TOA}$ over East Asia is higher than that over South Asia, and the difference of U/I aerosol $ARFE_{TOA}$ between continental sites and coastal/marine sites, are also evident. However, there are some discrepancies among the results by different methods at various sub-regions. For example, the $ARFE_{TOA}$ of BB aerosol is stronger than that of U/I aerosol in the 2-D approach using AAE and EAE (which is contrary to the results using SSA and EAE).

To facilitate the comparisons of various 2-D results with the MD results, Table 6 is given to estimate the differences in ARF and ARFE due to the use of different methods. For the ARF at the BOA and TOA, the 2-D minus MD difference is generally larger for the former than the later in terms of magnitude (both lower than 10 W/m^2). The ARF of dust aerosol mostly has the lowest disagreement among the various methods, while the reverse is true for the ARF of BB aerosol. For the ARFE, the difference between the 2-D and MD method is within 10%. The 2-D AAE-EAE method is found to induce larger differences for BB and U/I aerosols. It is noted that certain 2-D classifications bring about little changes in ARF and ARFE for some types of aerosols. However, the overall performance of 2-D classification is unstable and there is no easy way to decide on which 2-D method should be used.

Table 6. Daily averaged ARF (unit: W/m^2) and ARFE (unit: $\text{W/m}^2/\text{AOD}_{550\text{nm}}$) for various types of aerosols from MD method as well as the 2-D minus MD results for the whole study region.

	Aerosol Type	MD	2-D Minus MD Difference		
			SSA-EAE	RRI-EAE	AAE-EAE
ARF_{BOA}	BB	−104.4	6.3	7.4	10.0
	U/I	−85.7	−7.9	1.7	−6.4
	Dust	−88.2	−0.5	−4.1	−6.2
ARF_{TOA}	BB	−31.3	4.9	−3.4	−4.9
	U/I	−35.3	−2.4	−1.5	4.0
	Dust	−36.3	−2.9	−1.7	−1.6
$ARFE_{BOA}$	BB	−165.3	−13.8	10.4	14.8
	U/I	−140.5	−0.9	4.7	−14.3
	Dust	−146.1	5.0	−0.5	−0.5
$ARFE_{TOA}$	BB	−51.1	2.0	−3.2	−5.5
	U/I	−59.4	1.8	1.1	7.8
	Dust	−60.3	−2.4	0.2	2.0

5. Conclusions

Based on the aerosol properties retrieved by AERONET, the multi-dimensional MD method using five parameters (RRI, IRI, EAE, AAE, and SSA) as well as the 2-D aerosol classification method using three combinations of optical parameters (SSA and EAE, RRI and EAE, and AAE and EAE), are implemented to identify various types of aerosols and to investigate the corresponding ARF and ARFE for certain aerosol types over East and South Asia. The hierarchical clustering method is also used to analyze the land cover and background meteorological conditions for understanding the aerosol distributions.

The 2-D clustering method and multi-dimensional MD clustering method both capture some features of local aerosol types with strong seasonal and regional dependence. The NIGP area, SACOL site, Yulin site, the five sites in the Beijing area, the Ussuriysk site, and several sites in Korea are affected by dust aerosols to varying degrees in spring and summer and are also greatly affected by BB and U/I aerosols. The proportions of dust aerosols in spring at the SACOL site and in summer at sites near the NIGP area are the highest for all seasons. In spring, BB aerosols are dominant over the CIP area. In the Beijing area, Hong Kong area, Yangtze River Delta, CIP area, Hanoi area, Taiwan area, and Korea and Japan area, the proportion of U/I aerosols in summer greatly increases as compared with the other seasons. There are still large amounts of undetermined aerosols at various seasons and locations.

The MD method using multiple parameters is expected to reduce the influence of selected aerosol optical parameters by calculating a non-dimensional Mahalanobis distance to the centroids. For the MD method, the choice of centroids and distance for the clusters is important as each centroid represents a specific aerosol type and the distance minimizes the overlap between clusters, which essentially works similarly to the threshold range in the 2-D clustering method. The MD distance replaces the fixed thresholds and is considered more comprehensive in aerosol classification. Our results also reveal quite reasonable aerosol classifications through the MD method.

The 2-D clustering method is previously considered useful to distinguish the major types of aerosols with only two aerosol parameters. The performances of this method are largely dependent on the sets of parameters (SSA and EAE, AAE and EAE, and RRI and EAE) and thresholds, though similar results could be obtained. However, for the same region, the proportions of specific aerosol types classified by different sets of parameters are different. For example, the proportions of BB aerosol classified by the approach using RRI and AAE are much higher than those classified by the approach using SSA and EAE in Beijing and Korea. Additionally, certain sets of aerosol parameters could be limited in identifying aerosol types in some regions. The SSA and EAE, for example, are replaced by RRI and EAE for the Taiwan region due to the especially high SSA that causes difficulties in aerosol classification. Finally, the thresholds used to determine the aerosol types are critical to deciding the exact proportions of each type of aerosol. For example, the high EAE feature of the aerosols in the CIP region results in more undetermined aerosols, as the local EAE exceeds the thresholds.

A detailed comparison of the results from the 2-D aerosol classification with those from the MD classification reveals the existence of large proportions of undetermined aerosols in MD results which could be mistakenly attributed to BB or U/I aerosols in the 2-D results instead. Among all the identifiable dust aerosol samples, the three 2-D methods all classified near half of the total samples. The 2-D RRI-EAE and the 2-D AAE-EAE methods can classify about half of the total U/I and BB aerosols, respectively. However, none of the 2-D methods could provide reliable aerosol classification results similar as the MD method.

The ARF and the ARFE at the TOA and BOA of various aerosol types classified by the MD and 2-D method have been estimated based on AERONET aerosol retrievals. Apart from the undetermined aerosols, it is evident that dust (-51 to -31 W/m^2) and marine (-85 to -21 W/m^2) aerosols always contribute most to the daily averaged ARF_{TOA} whenever they are present, followed by U/I (-50 to -22 W/m^2) and BB aerosols (-51 to -15 W/m^2). The $ARFE_{BOA}$ of BB aerosol is the strongest among those of other aerosol types. The differences in the ARFE for the same type of aerosol in various regions are indicative of the differences in the compositions of aerosol. As the proportions of various types of aerosols are somewhat different using various 2-D methods and the MD method, there still exist some differences in the ARF and ARFE. Such differences are estimated to be generally less than 10 W/m^2 for the ARF_{TOA} and ARF_{BOA} , and less than 10% for the $ARFE_{TOA}$ and $ARFE_{BOA}$.

Although the 2-D aerosol classification method with various sets of parameters and thresholds as well as a multi-dimensional MD method are used and compared, there is a lack of observed aerosol types to be compared with in this study. For the 2-D aerosol classification method, a more in-depth analysis of the aerosol parameters and the related thresholds to be used is urgently needed. For the MD method, the choice of centroids and distances should undergo more rigorous training for global application. More knowledge about the compositions of the various aerosol types (including the undetermined aerosols) could be helpful to improve the understanding of the ARF and ARFE. Our results could be useful for validation of satellite observations and model simulations.

Supplementary Materials: The following supporting information can be downloaded at <https://www.mdpi.com/article/10.3390/rs14092058/s1>. Table S1. The differences in the percentages of individual aerosol types between 2-D and MD results (unit: %). For each sub-region, the 3 values (from top to bottom) in the “difference” column refers to the percentage difference between the results of 2-D SSA-EAE and MD, 2-D RRI-EAE and MD, and 2-D AAE-EAE and MD, respectively. Table S2. The differences in the ARF_{TOA} ($ARFE_{TOA}$) of individual aerosol types between 2-D and MD results (unit: W/m^2 and $W/m^2/AOD_{550nm}$). For each sub-region, the 3 values (from top to bottom) in the “difference” column refers to the ARF (ARFE) difference between the results of 2-D SSA-EAE and MD, 2-D RRI-EAE and MD, and 2-D AAE-EAE and MD, respectively. Note the values in the parenthesis indicate the ARFE. Table S3. The same as Table S2 except that ARF_{BOA} ($ARFE_{BOA}$) are shown. Figure S1. Seasonal and annual averaged meteorological conditions for the period of March 1998 to February 2018: (a) spring (March, April and May); (b) summer (June, July and August); (c) autumn (September, October and November); (d) winter (December, January and February) and (e) annual. The arrow represents wind field at 1000 hPa, and the shaded represents the precipitation (Unit: mm/d). Figure S2. The aerosol types at the AERONET sites (a–r) in IP identified by the 2-D clustering method with AAE and EAE for the period of March 1998 to February 2018. The blue asterisks on the map indicates the locations of the sites with enough valid data for analysis, while the black ones represent the sites that are not used. The green, red, yellow, and blue dots on the scatter plots represent the data in boreal spring (March, April, and May), summer (June, July, and August), autumn (September, October, and November), and winter (December, January, and February), respectively. The boxes plotted with dash lines indicate the sub-regions listed in Table 4. For each sub-region, the differences in per-centage (2-D result minus MD result) for the U/I, BB, dust, and undetermined aerosols are shown respectively. Figure S3. The same as Figure S2 but for the aerosol classification by the 2-D clustering method using SSA and EAE at the AERONET sites (a–l) in Japan, Korea and southeast Russia. Figure S4. The daily averaged ARF_{TOA} for various aerosol types based on (a) the MD method; (b) the 2-D SSA-EAE method; (c) the 2-D RRI-EAE method; (d) the 2-D AAE-EAE method (Unit: W/m^2). Figure S5. The same as Figure S4 except that the daily averaged ARF_{BOA} are shown. Figure S6. The daily averaged $ARFE_{TOA}$ for various aerosol types based on (a) the MD method; (b) the 2-D SSA-EAE method; (c) the 2-D RRI-EAE method; (d) the 2-D AAE-EAE method (Unit: $W/m^2/AOD_{550nm}$). Figure S7. The same as Figure S6 except that the daily averaged $ARFE_{BOA}$ are show.

Author Contributions: Conceptualization, Y.L. and B.Y.; methodology, Y.L.; validation, Y.L. and B.Y.; formal analysis, Y.L. and B.Y.; investigation, Y.L. and B.Y.; data curation, Y.L.; visualization, Y.L.; writing—original draft, Y.L.; funding acquisition, B.Y.; supervision, B.Y.; writing—review and editing, B.Y. All authors have read and agreed to the published version of the manuscript.

Funding: This study was partially supported by the Natural Science Foundation of Guangdong Province (2019A1515011230) and the funding to the Guangdong Province Key Laboratory for Climate Change and Natural Disaster Studies (2020B1212060025). Bingqi Yi acknowledges the support from the Pearl River Talents Program of the Department of Science and Technology of Guangdong Province (2017GC010619).

Data Availability Statement: No new data were created in this study. Data sharing is not applicable to this article.

Acknowledgments: We thank the NASA/Goddard Space Flight Center (NASA/GSFC) for providing the TMPA data (https://disc.gsfc.nasa.gov/datasets/TRMM_3B42_Daily_7/summary, accessed on 15 March 2022) and the ECMWF for the ERA-Interim data. We also thank the MODIS project and

AERONET project (<http://aeronet.gsfc.nasa.gov/>, accessed on 15 March 2022) for providing the data used in this work. Further, we thank the principal investigators and co-investigators and their staff for establishing and maintaining the sites used in this investigation.

Conflicts of Interest: The authors declare no conflict of interest.

Appendix A

Appendix A shows the process of hierarchical cluster analysis and the use of the silhouette coefficient. The hierarchical clustering method is used to identify the meteorological features and to divide regions with similar meteorological conditions. The silhouette coefficient [39] is used to determine the desired number of clusters.

In this study, the meteorological factors are standardized as follows:

$$y = \frac{x - \mu}{\sigma} \quad (\text{A1})$$

where μ is the mean value of a meteorological factor, σ is the standard deviation, x is the value of the meteorological factor, and y is the standardized factor.

The key is how to calculate the distance between clusters, which means the distance between sample sets. Given the clusters Cl_i and Cl_j , the averaged distance (d_{avg}) of the two sets of observations (two groups of grid points) x_i and z_j can be calculated as:

$$d_{avg}(Cl_i, Cl_j) = \frac{1}{|Cl_i||Cl_j|} \sum_{x_i \in Cl_i} \sum_{z_j \in Cl_j} \text{dist}_{ed}(x_i, z_j) \quad (\text{A2})$$

where dist_{ed} indicates the Euclidean distance between two samples x and z which belong to the Cl_i and Cl_j clusters, respectively. Given $x_i = (x_{i1}, x_{i2}, \dots, x_{in})^T$ and $z_j = (z_{j1}, z_{j2}, \dots, z_{jn})^T$ where x_{in} and z_{jn} are the attributes (PR, RH, TCC, U, V and T) of two sample points x_i and z_j , respectively, the Euclidean distance $\text{dist}_{ed}(*, *)$ is calculated as followed:

$$\text{dist}_{ed}(x_i, z_j) = \sqrt{\sum_{u=1}^n |x_{iu} - z_{ju}|^2} \quad (\text{A3})$$

A key benefit of hierarchical clustering is that it could generate any number of clusters, but it is a challenge to choose an appropriate number as it is important to find a balance between the dissimilarity of clusters and the similarity of samples within clusters.

The silhouette coefficient combines the cohesion and separation of clustering to evaluate the clustering effect. The silhouette coefficient $S(i)$ for the sample point x_i in the cluster Cl_i is defined as follows:

$$S(i) = \frac{\text{sn}(i) - \text{sm}(i)}{\max(\text{sm}(i), \text{sn}(i))} \quad (\text{A4})$$

where $\text{sm}(i)$ represents the intra-cluster dissimilarity (cohesion) of the sample point x_i , and $\text{sn}(i)$ represents the inter-cluster dissimilarity (separation) of the sample point x_i . Here, $\text{sm}(i)$ is the averaged distance between the sample point x_i and the other sample points in the cluster Cl_i , while $\text{sn}(i)$ is the minimum value of $\text{sn}_j(i)$ where $\text{sn}_j(i)$ is the averaged distance between the sample point x_i and all sample points in the other cluster Cl_j . Note the distance mentioned here refers to the Euclidean distance (Equation (A3)). Generally, the silhouette coefficient $S(i)$ ranges from -1 to 1 . The negative $S(i)$ usually indicates that the sample point is assigned to the wrong cluster, while the $S(i)$ closes to 1 indicates that the sample point is properly classified. The mean $S(i)$ of all sample points is the silhouette coefficient of clustering result S . If S is close to 1 , the number of clustering classification is considered reasonable.

References

1. Boucher, O.; Randall, D.; Artaxo, P.; Bretherton, C.; Feingold, G.; Forster, P.; Kerminen, V.M.; Kondo, Y.; Liao, H.; Lohmann, U.; et al. Clouds and aerosols. In *Climate Change 2013: The Physical Science Basis. Contribution of Working Group I to the Fifth Assessment Report of the Intergovernmental Panel on Climate Change*; Stocker, T.F., Qin, D., Plattner, G.K., Tignor, M., Allen, S.K., Boschung, J., Nauels, A., Xia, Y., Bex, V., Midgley, P.M., Eds.; Cambridge University Press: Cambridge, UK; New York, NY, USA, 2013.
2. Sakerin, S.M.; Pavlov, A.N.; Bukin, O.A.; Kabanov, D.M.; Kornienko, G.I.; Pol'kin, V.V.; Stolyarchuk, S.Y.; Turchinovich, Y.S.; Shmirko, K.A.; Mayor, A.Y. Results of an integrated aerosol experiment in the continent-ocean transition zone (Primorye and the Sea of Japan); Part 1: Variations of atmospheric aerosol optical depth and vertical profiles. *Atmos. Ocean. Opt.* **2011**, *24*, 64–73. [[CrossRef](#)]
3. Hsu, C.Y.; Chiang, H.C.; Lin, S.L.; Chen, M.J.; Lin, T.Y.; Chen, Y.C. Elemental characterization and source apportionment of PM10 and PM2.5 in the western coastal area of central Taiwan. *Sci. Total Environ.* **2015**, *541*, 1139–1150. [[CrossRef](#)]
4. Duc, H.N.; Bang, H.Q.; Quan, N.H.; Quang, N.X. Impact of biomass burnings in Southeast Asia on air quality and pollutant transport during the end of the 2019 dry season. *Environ. Monit. Assess.* **2021**, *193*, 565. [[CrossRef](#)] [[PubMed](#)]
5. Lei, Y.L.; Shen, Z.X.; Wang, Q.Y.; Zhang, T.; Cao, J.J.; Sun, J.; Zhang, Q.; Wang, L.Q.; Xu, H.M.; Tian, J.; et al. Optical characteristics and source apportionment of brown carbon in winter PM_{2.5} over Yulin in Northern China. *Atmos. Res.* **2018**, *213*, 27–33. [[CrossRef](#)]
6. Twomey, S. Influence of Pollution on the Shortwave Albedo of Clouds. *J. Atmos. Sci.* **1977**, *34*, 1149–1152. [[CrossRef](#)]
7. Li, Z.Q.; Lau, W.K.M.; Ramanathan, V.; Wu, G.; Ding, Y.; Manoj, M.G.; Liu, J.; Qian, Y.; Li, J.; Zhou, T.; et al. Aerosol and monsoon climate interactions over Asia. *Rev. Geophys.* **2016**, *54*, 866–929. [[CrossRef](#)]
8. Hua, Y.; Wang, S.X.; Jiang, J.K.; Zhou, W.; Xu, Q.C.; Li, X.X.; Liu, B.X.; Zhang, D.W.; Zheng, M. Characteristics and sources of aerosol pollution at a polluted rural site southwest in Beijing, China. *Sci. Total Environ.* **2018**, *626*, 519–527. [[CrossRef](#)]
9. Mishra, A.K.; Shibata, T. Synergistic analyses of optical and microphysical properties of agricultural crop residue burning aerosols over the Indo-Gangetic Basin (IGB). *Atmos. Environ.* **2012**, *57*, 205–218. [[CrossRef](#)]
10. Kim, Y.J. Asian Dust particles impacts on air quality and radiative forcing over Korea. In *IOP Conference Series: Earth and Environmental Science*; IOP Publishing: Bristol, UK, 2009; Volume 7, p. 012005. [[CrossRef](#)]
11. Guo, J.; Deng, M.J.; Lee, S.S.; Wang, F.; Li, Z.Q.; Zhai, P.M.; Liu, H.; Lv, W.T.; Yao, W.; Li, X.W. Delaying precipitation and lightning by air pollution over the Pearl River Delta. Part I: Observational analyses. *J. Geophys. Res. Atmos.* **2016**, *121*, 6472–6488. [[CrossRef](#)]
12. Liu, Y.U.; Sun, J.R.; Yang, B. The effects of black carbon and sulphate aerosols in China regions on East Asia monsoons. *Tellus* **2009**, *61*, 642–656. [[CrossRef](#)]
13. Jiang, J.H.; Su, H.; Huang, L.; Wang, Y.; Massie, S.; Zhao, B.; Omar, A.; Wang, Z.E. Contrasting effects on deep convective clouds by different types of aerosols. *Nat. Commun.* **2018**, *9*, 3874. [[CrossRef](#)]
14. Holben, B.N.; Eck, T.F.; Slutsker, I.; Smirnov, A.; Sinyuk, A.; Schafer, V.; Giles, D.; Dubovik, O. Aeronet's Version 2.0 quality assurance criteria. *Remote Sens. Atmos. Clouds* **2006**, *6408*, 64080Q. [[CrossRef](#)]
15. Che, H.Z.; Zhang, X.Y.; Chen, H.B.; Damiri, B.; Goloub, P.; Li, Z.Q.; Zhang, X.C.; Wei, Y.; Zhou, H.G.; Dong, F.; et al. Instrument calibration and aerosol optical depth validation of the China aerosol remote sensing network. *J. Geophys. Res. Atmos.* **2009**, *114*, D03206. [[CrossRef](#)]
16. Li, Z.Q.; Xu, H.; Li, K.T.; Li, D.H.; Xie, Y.S.; Li, L.; Zhang, Y.; Gu, X.F.; ZHao, W.; Tian, Q.J.; et al. Comprehensive study of optical, physical, chemical, and radiative properties of total columnar atmospheric aerosols over China: An overview of sun-Sky radiometer observation network measurements. *Bull. Amer. Meteor. Soc.* **2018**, *99*, 739–755. [[CrossRef](#)]
17. Hamill, P.; Giordano, M.; Ward, C.; Giles, D.; Holbene, B. An AERONET-Based aerosol classification using the Mahalanobis distance. *Atmos. Environ.* **2016**, *140*, 213–233. [[CrossRef](#)]
18. Li, Z.; Zhang, Y.; Xu, H.; Li, K.; Dubovik, O.; Goloub, P. The Fundamental Aerosol Models over China Region: A Cluster Analysis of the Ground-Based Remote Sensing Measurements of Total Columnar Atmosphere. *Geophys. Res. Lett.* **2019**, *46*, 4924–4932. [[CrossRef](#)]
19. Zheng, Y.; Che, H.Z.; Xia, X.G.; Wang, Y.Q.; Yang, L.K.; Chen, J.; Wang, H.; Zhao, H.J.; Li, L.; Zhang, L.; et al. Aerosol optical properties and its type classification based on multiyear joint observation campaign in north China plain megalopolis. *Chemosphere* **2020**, *273*, 128560. [[CrossRef](#)] [[PubMed](#)]
20. Chen, H.; Cheng, T.H.; Gu, X.F.; Wu, Y. Characterization of aerosols in Beijing during severe aerosol loadings. *Atmos. Environ.* **2015**, *119*, 273–281. [[CrossRef](#)]
21. Bibi, H.; Alam, K.; Bibi, S. In-depth discrimination of aerosol types using multiple clustering techniques over four locations in Indo-Gangetic plains. *Atmos. Res.* **2016**, *181*, 106–114. [[CrossRef](#)]
22. Russell, P.B.; Bergstrom, R.W.; Shinzuka, Y.; Clarke, A.D.; DeCarlo, P.F.; Jimenez, J.L.; Livingston, J.M.; Redemann, J.; Dubovik, O.; Strawa, A. Absorption Angstrom Exponent in AERONET and related data as an indicator of aerosol composition. *Atmos. Chem. Phys.* **2010**, *10*, 1155–1169. [[CrossRef](#)]
23. Xia, X.G.; Li, Z.Q.; Holben, B.; Wang, P.C.; Eck, T.; Chen, H.B.; Cribb, M.; Zhao, Y.X. Aerosol optical properties and radiative effects in the Yangtze Delta region of China. *J. Geophys. Res.* **2007**, *112*, D22S12. [[CrossRef](#)]
24. Lau, K.M.; Kim, M.K.; Kim, K.M. Asian summer monsoon anomalies induced by aerosol direct forcing: The role of the Tibetan Plateau. *Clim. Dyn.* **2006**, *26*, 855–864. [[CrossRef](#)]
25. Liu, J.J.; Zheng, Y.F.; Li, Z.Q.; Flynn, C.; Cribb, M. Seasonal variations of aerosol optical properties, vertical distribution and associated radiative effects in the Yangtze Delta region of China. *J. Geophys. Res. Atmos.* **2012**, *117*, D00K38. [[CrossRef](#)]

26. Gautam, R.; Hsu, N.C.; Tsay, S.C.; Lau, K.M.; Holben, B.; Bell, S.; Smirnov, A.; Li, C.; Hansell, R.; Ji, Q.; et al. Accumulation of aerosols over the Indo-Gangetic plains and southern slopes of the Himalayas: Distribution, properties and radiative effects during the 2009 pre-monsoon season. *Atmos. Chem. Phys.* **2011**, *11*, 12841–12863. [[CrossRef](#)]
27. Pavlidis, V.; Katragkou, E.; Prein, A.; Georgoulias, A.K.; Kartsios, S.; Zanis, P.; Karacostas, T. Investigating the sensitivity to resolving aerosol interactions in downscaling regional model experiments with WRFv3.8.1 over Europe. *Geosci. Model Dev.* **2020**, *13*, 2511–2532. [[CrossRef](#)]
28. Wang, H.; Zhang, X.Y.; Gong, S.L.; Chen, Y.; Shi, G.Y.; Li, W. Radiative feedback of dust aerosols on the East Asian dust storms. *J. Geophys. Res.* **2010**, *115*, D23214. [[CrossRef](#)]
29. Déandreis, C.; Balkanski, Y.; Dufresne, J.L.; Cozic, A. Radiative forcing estimates of sulfate aerosol in coupled climate-chemistry models with emphasis on the role of the temporal variability. *Atmos. Chem. Phys.* **2012**, *12*, 5583–5602. [[CrossRef](#)]
30. Li, L.; Li, Z.; Li, K.; Wang, Y.; Tian, Q.; Su, X.; Yang, L.; Ye, S.; Xu, H. Aerosol Direct Radiative Effects over China Based on Long-Term Observations within the Sun–Sky Radiometer Observation Network (SONET). *Remote Sens.* **2020**, *12*, 3296. [[CrossRef](#)]
31. Markowicz, K.M.; Zawadzka-Manko, O.; Lisok, J.; Chilinski, M.T.; Xian, P. The impact of moderately absorbing aerosol on surface sensible, latent, and net radiative fluxes during the summer of 2015 in Central Europe. *J. Aerosol. Sci.* **2020**, *151*, 105627. [[CrossRef](#)]
32. García, O.E.; Díaz, J.P.; Expósito, F.J.; Díaz, A.M.; Dubovik, O.; Derimian, Y.; Dubuisson, P.; Roger, J.C. Shortwave radiative forcing and efficiency of key aerosol types using AERONET data. *Atmos. Chem. Phys.* **2012**, *12*, 5129–5145. [[CrossRef](#)]
33. Dubovik, O.; Holben, B.; Eck, T.F.; Smirnov, A.; Kaufman, Y.J.; King, M.D.; Tanré, D.; Slutsker, I. Variability of absorption and optical properties of key aerosol types observed in worldwide locations. *J. Atmos. Sci.* **2002**, *59*, 590–608. [[CrossRef](#)]
34. Latha, R.; Murthy, B.S.; Kumar, M.; Lipi, K.; Jyotsna, S. Aerosol radiative forcing controls: Results from an Indian table-top mining region. *Atmos. Environ.* **2013**, *81*, 687–694. [[CrossRef](#)]
35. Sulla-Menashe, D.; Gray, J.M.; Abercrombie, S.P.; Friedla, M.A. Hierarchical mapping of annual global land cover 2001 to present: The MODIS Collection 6 Land Cover product. *Remote Sens. Environ.* **2019**, *222*, 183–194. [[CrossRef](#)]
36. Dee, D.P.; Uppala, S.M.; Simmons, A.J.; Berrisford, P.; Poli, P.; Kobayashi, S.; Andrae, U.; Balmaseda, M.A.; Balsamo, G.; Bauer, P.; et al. The ERA-Interim reanalysis: Configuration and performance of the data assimilation system. *Q. J. R. Meteorol. Soc.* **2011**, *137*, 553–597. [[CrossRef](#)]
37. Huffman, G.J.; Bolvin, D.T.; Nelkin, E.J.; Adler, R.F. *TRMM (TMPA) Precipitation L3 1 Day 0.25 Degree X 0.25 Degree V7*; Andrey, S., Ed.; Goddard Earth Sciences Data and Information Services Center (GES DISC), 2016. Available online: https://disc.gsfc.nasa.gov/datasets/TRMM_3B42_Daily_7/summary (accessed on 15 March 2022). [[CrossRef](#)]
38. Fox, W.R. *Review of Finding Groups in Data: An Introduction to Cluster Analysis*; Kaufman, L., Rousseeuw, P.J., Eds.; Journal of the Royal Statistical Society. Series C; Wiley: Hoboken, NJ, USA, 1991; Volume 40, pp. 486–487. [[CrossRef](#)]
39. Rousseeuw, P.J. Silhouettes: A graphical aid to the interpretation and validation of cluster analysis. *J. Comput. Appl. Math.* **1987**, *20*, 53–65. [[CrossRef](#)]
40. Mahalanobis, P.C. On the generalized distance in statistics. *Proc. Natl. Inst. Sci. India* **1936**, *2*, 49–55.
41. Huang, K.; Fu, J.S.; Hsu, N.C.; Gao, Y.; Dong, X.Y.; Tsay, S.C.; Lam, Y.F. Impact assessment of biomass burning on air quality in Southeast and East Asia during BASE-ASIA. *Atmos. Environ.* **2013**, *78*, 291–302. [[CrossRef](#)]
42. Ding, Y.H.; Chan, J. The East Asian summer monsoon: An overview. *Meteorol. Atmos. Phys.* **2005**, *89*, 117–142. [[CrossRef](#)]
43. Prijith, S.S.; Babu, S.S.; Lakshmi, N.B.; Sathesh, S.K.; Moorthy, K.K. Meridional gradients in aerosol vertical distribution over Indian Mainland: Observations and model simulations. *Atmos. Environ.* **2016**, *125*, 337–345. [[CrossRef](#)]
44. Kansakar, S.R.; Hannah, D.M.; Gerrard, J.; Rees, R. Spatial pattern in the precipitation regime of Nepal. *Int. J. Climatol.* **2004**, *24*, 1645–1659. [[CrossRef](#)]
45. Li, J.; Zhang, Y.Q.; Wang, Z.F.; Sun, Y.L.; Fu, P.Q.; Yang, Y.C.; Huang, H.L.; Li, J.J.; Zhang, Q.; Lin, C.Y.; et al. Regional impact of biomass burning in Southeast Asia on atmospheric aerosols during the 2013 Seven South-East Asian Studies Project. *Aerosol Air Qual. Res.* **2017**, *17*, 2924–2941. [[CrossRef](#)]
46. Kozlov, V.S.; Pol'kin, V.V.; Panchenko, M.V.; Golobokova, L.P.; Turchinovich, U.S.; Hodzher, T.V. Results of integrated aerosol experiment in the continent-ocean transition zone (Primorye and the Japan Sea). Part 3. Microphysical characteristics and ion composition of aerosol in the near-ground and near-water layers. *Atmos. Ocean. Opt.* **2011**, *24*, 207–217. [[CrossRef](#)]
47. Ozdemir, E.; Tuygun, G.T.; Elbir, T. Application of aerosol classification methods based on AERONET version 3 product over eastern Mediterranean and Black Sea. *Atmos. Pollut. Res.* **2020**, *11*, 2226–2243. [[CrossRef](#)]
48. Zhang, L.; Zheng, X.S. Spatial-temporal Variation of Aerosol Optical Properties in Coastal Region, China Based on CALIPSO Data. *J. Earth Sci. Environ.* **2021**, *43*, 1033–1049. [[CrossRef](#)]
49. Dementeva, A.; Zhamsueva, G.; Zayakhanov, A.; Tsydyrov, V. Interannual and Seasonal Variation of Optical and Microphysical Properties of Aerosol in the Baikal Region. *Atmosphere* **2022**, *13*, 211. [[CrossRef](#)]
50. Stefan, S.; Voinea, S.; Iorga, G. Study of the aerosol optical characteristics over the Romanian Black Sea Coast using AERONET data. *Atmos. Pollut. Res.* **2020**, *11*, 1165–1178. [[CrossRef](#)]
51. Cuneo, L.; Ulke, A.G.; Cerne, B. Advances in the characterization of aerosol optical properties using long-term data from AERONET in Buenos Aires. *Atmos. Pollut. Res.* **2022**, *13*, 101360. [[CrossRef](#)]
52. Rupakheti, D.; Adhikary, B.; Praveen, P.S.; Rupakheti, M.; Kang, S.C.; Mahata, K.S.; Naja, M.; Zhang, Q.G.; Panday, A.K.; Lawrence, M.G. Pre-monsoon air quality over Lumbini, a world heritage site along the Himalayan foothills. *Atmos. Chem. Phys.* **2017**, *17*, 11041–11063. [[CrossRef](#)]

53. Rupakheti, D.; Kang, S.C.; Rupakheti, M.; Cong, Z.Y.; Tripathee, L.; Panday, A.K.; Holben, B.N. Observation of optical properties and sources of aerosols at Buddha's birthplace, Lumbini, Nepal: Environmental implications. *Environ. Sci. Pollut. Res.* **2018**, *25*, 14868–14881. [[CrossRef](#)] [[PubMed](#)]
54. Cao, C.X.; Zheng, S.; Singh, R.P. Characteristics of aerosol optical properties and meteorological parameters during three major dust events (2005–2010) over Beijing, China. *Atmos. Res.* **2014**, *150*, 129–142. [[CrossRef](#)]
55. Du, C.L.; Li, X.M.; Chen, C.; Wang, F.Q.; Peng, Y.; Dong, Y.; Dong, Z.P. Concentration variation and absorption characteristics of black carbon during autumn and winter in Yulin near Mu Us Sandy Land. *J. Desert Res.* **2014**, *34*, 869–877. [[CrossRef](#)]
56. Yan, C.Q.; Zheng, M.; Sullivan, A.P.; Bosch, C.; Desyaterik, Y.; Andersson, A.; Li, X.Y.; Guo, X.S.; Zhou, T.; Gustafsson, Ö.; et al. Chemical characteristics and light-absorbing property of water-soluble organic carbon in Beijing: Biomass burning contributions. *Atmos. Environ.* **2015**, *121*, 4–12. [[CrossRef](#)]
57. You, C.; Gao, S.P.; Xu, C. Biomass burning emissions contaminate winter snowfalls in urban Beijing: A case study in 2012. *Atmos. Pollut. Res.* **2015**, *6*, 376–381. [[CrossRef](#)]
58. Yang, Y.; Li, X.R.; Shen, R.R.; Liu, Z.R.; Ji, D.S.; Wang, Y.S. Seasonal variation and sources of derivatized phenols in atmospheric fine particulate matter in North China Plain. *J. Atmos. Sci.* **2020**, *89*, 139–147. [[CrossRef](#)]
59. Cheng, Y.; Engling, G.; He, K.B.; Duan, F.K.; Ma, Y.L.; Du, Z.Y.; Liu, J.M.; Zheng, M.; Weber, R.J. Biomass burning contribution to Beijing aerosol. *Atmos. Chem. Phys.* **2013**, *13*, 7765–7781. [[CrossRef](#)]
60. Emilenko, A.S.; Isakov, A.A.; Kopeikin, V.M.; Wang, G.C. Relative contributions of regional, urban, and local sources of atmospheric aerosol pollution in regions with different levels of anthropogenic load. In *21st International Symposium Atmospheric and Ocean Optics: Atmospheric Physics*; SPIE: Bellingham, WA, USA, 2015; Volume 9680, p. 968046. [[CrossRef](#)]
61. Dong, X.; Fu, J.S. Understanding interannual variations of biomass burning from Peninsular Southeast Asia, part II: Variability and different influences in lower and higher atmosphere levels. *Atmos. Environ.* **2015**, *115*, 9–18. [[CrossRef](#)]
62. Sang, X.F.; Chan, C.Y.; Engling, G.; Chan, L.Y.; Wang, X.M.; Zhang, Y.N.; Shi, S.; Zhang, Z.S.; Zhang, T.; Hu, M. Levoglucosan enhancement in ambient aerosol during springtime transport events of biomass burning smoke to southeast China. *Tellus B Chem. Phys. Meteorol.* **2011**, *63*, 129–139. [[CrossRef](#)]
63. Ding, A.; Wang, T.; Fu, C. Transport characteristics and origins of carbon monoxide and ozone in Hong Kong, south China. *J. Geophys. Res. Atmos.* **2013**, *118*, 9475–9488. [[CrossRef](#)]
64. Logan, T.; Xi, B.K.; Dong, X.Q. A Comparison of the Mineral Dust Absorptive Properties between Two Asian Dust Events. *Atmosphere* **2015**, *4*, 1–16. [[CrossRef](#)]
65. Choi, J.K.; Heo, J.B.; Ban, S.J.; Yi, S.M.; Zoh, K.D. Source apportionment of PM_{2.5} at the coastal area in Korea. *Sci. Total Environ.* **2013**, *447*, 370–380. [[CrossRef](#)]
66. Shon, Z.H. Long-term variations in PM_{2.5} emission from open biomass burning in Northeast Asia derived from satellite-derived data for 2000–2013. *Atmos. Environ.* **2015**, *107*, 342–350. [[CrossRef](#)]
67. Titos, G.; Burgos, M.A.; Zieger, P.; Alados-Arboledas, L.; Baltensperger, U.; Jefferson, A.; Sherman, J.; Weingartner, E.; Henzing, B.; Luoma, K.; et al. A global study of hygroscopicity-driven light-scattering enhancement in the context of other in situ aerosol optical properties. *Atmos. Chem. Phys.* **2021**, *21*, 13031–13050. [[CrossRef](#)]
68. Yoon, S.C.; Kim, J. Influences of relative humidity on aerosol optical properties and aerosol radiative forcing during ACE-Asia. *Atmos. Environ.* **2006**, *40*, 4328–4338. [[CrossRef](#)]